

ESD-TR-65-553  
ESTI FILE COPY

ESD-TDR-65-553

# ESD RECORD COPY

RETURN TO  
SCIENTIFIC & TECHNICAL INFORMATION DIVISION  
(ESTI), BUILDING 1211

## ESD ACCESSION LIST

ESTI Call No. AL 49500  
Copy No. 1 of 1 cys.

3

### Solid State Research

1965

Prepared under Electronic Systems Division Contract AF 19(628)-5167 by

## Lincoln Laboratory

MASSACHUSETTS INSTITUTE OF TECHNOLOGY

Lexington, Massachusetts



*ESRL*

*AD0629093*

The work reported in this document was performed at Lincoln Laboratory, a center for research operated by Massachusetts Institute of Technology, with the support of the U.S. Air Force under Contract AF 19(628)-5167.

This report may be reproduced to satisfy needs of U.S. Government agencies.

Distribution of this document is unlimited.

Non-Lincoln Recipients

**PLEASE DO NOT RETURN**

Permission is given to destroy this document when it is no longer needed.

3

Solid State Research

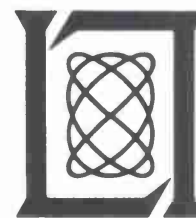
1965

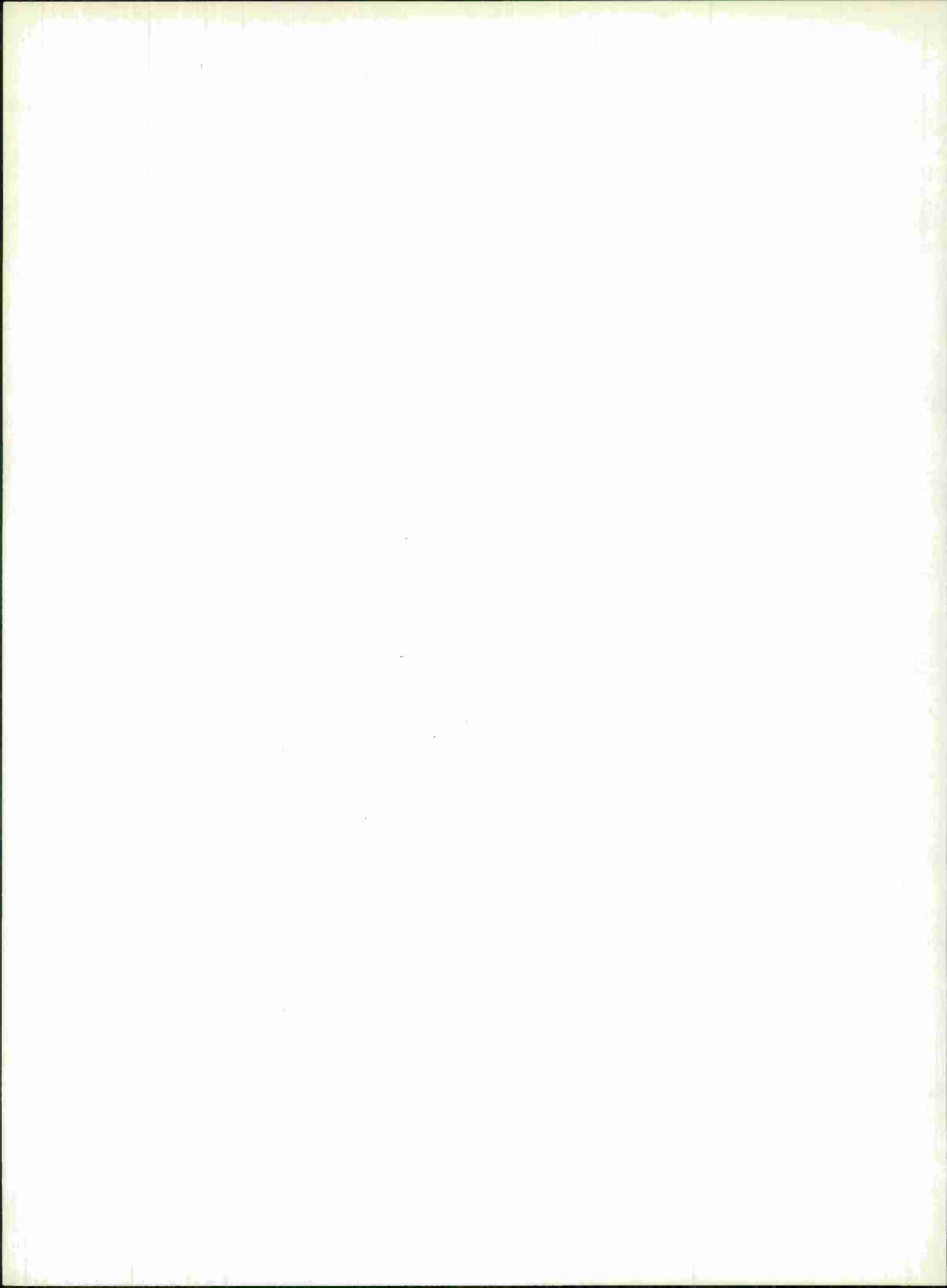
Issued 14 February 1966

Lincoln Laboratory

MASSACHUSETTS INSTITUTE OF TECHNOLOGY

Lexington, Massachusetts





#### ABSTRACT

This report covers in detail the solid state research work at Lincoln Laboratory for the period 1 August through 31 October 1965. The topics covered are Solid State Device Research, Laser Research, Materials Research, and Physics of Solids.

Accepted for the Air Force  
Franklin C. Hudson  
Chief, Lincoln Laboratory Office

# INTRODUCTION

## I. SOLID STATE DEVICE RESEARCH

The output wavelength of PbSe diode lasers operating at 77°K has been tuned in the range from 7.5 to over 22 $\mu$  by applying hydrostatic pressures of up to 14 kbar. Extension to wavelengths above 13 $\mu$  was made possible by the development of polycrystalline germanium and silicon windows capable of withstanding the high pressures involved. These windows have been tested to 20 kbar with no evidence of deterioration. Germanium windows were used in the wavelength range to 20 $\mu$  in order to eliminate transmission difficulties due to lattice absorption bands in silicon; above 20 $\mu$ , where germanium has lattice absorption bands, silicon windows were used. Our range of tuning has been limited because the helium pressure-transmitting fluid freezes at  $14.15 \pm 0.03$  kbar at 77°K. Since hydrostatic pressure cannot be transmitted reliably through solid helium, we plan to extend the diode emission to longer wavelengths by first pressurizing the system to above 14 kbar at room temperature (where helium is still a gas), and then cooling it to 77°K and below. With constant current through the diode, an increasing pressure has been observed to produce no significant change in the intensity of either the coherent or spontaneous emission, until the freezing point of helium is reached. The large reduction in the intensity of emission that occurred when the helium froze is attributed to diffuse scattering of the radiation by the solid helium.

A new technique has been developed for growing a thin layer of InSb on an InSb substrate from a saturated In-InSb melt. This type of growth from a solution has been previously used in the fabrication of GaAs and Ge p-n junctions; however, at the lower temperatures required for InSb (about 300°C), certain modifications were made, such as the use of hot liquid stearic acid which covers the InSb substrate and the In-InSb melt during the growth process. By suitably doping the melt, uniform planar InSb  $n^+$ -p junctions were grown on substrate areas of about 2 cm<sup>2</sup>. Such InSb junctions have been used in large-volume injection lasers which emit coherent light in a direction normal to the junction plane.

Injection of carriers into InSb  $n^+pp^+$  structures similar to those used as bulk lasers has been studied by determining the distribution of potential and electric field along the p-region at various current levels. Measurements were made using a movable potential probe with the sample at 77°K. These measurements indicate that at currents of less than 1 A/cm<sup>2</sup> the dominating mechanism is the injection of electrons into the p-region from the  $n^+$  contact, which causes a saturation of electron traps and an increased lifetime in the p-type bulk. At higher currents an appreciable number of holes is injected from the  $p^+$  region in order to neutralize the large number of injected electrons. This changeover from "single" to "double" injection produces changes in the potential distribution as well as changes in the region of bulk InSb from which the laser radiation is emitted.

Microwave amplification has been observed in bulk n-GaAs at room temperature. The samples were 50- $\mu$ -thick rectangular parallelepipeds with a mobility of about 5000 cm<sup>2</sup>/V-sec

and a resistivity of approximately 100 ohm-cm. The frequency at which the maximum gain occurs agrees fairly well with the frequency at which Gunn oscillations occur in lower resistivity samples ( $\sim 1$  ohm-cm) of the same thickness, but the average applied electric field necessary for gain is about 7000 V/cm — about twice the value usually required for Gunn oscillations. The amplifier sample exhibits only a slight tendency toward current saturation with increasing voltage, whereas the oscillator sample begins to saturate even below the threshold of oscillation, and above threshold exhibits a range of current oscillation relatively independent of voltage. The existence of a positive resistance in the amplifier samples for average applied electric fields much higher than the field at which Gunn oscillation normally occurs suggests that the usual domain formation does not take place in these high-resistivity samples. This agrees with recent calculations of McCumber and Chynoweth who have found that, for sufficiently small products of carrier concentration and sample length, the transferred electron effect leads to a negative conductance at frequencies near the reciprocal of the transit time, even though the DC solution displays only positive resistance.

## II. LASER RESEARCH

Absolute (nonconvective) instabilities were not found from an analysis of the dispersion relation for Stokes and anti-Stokes modes in an infinite Raman-active medium. Absolute instabilities were found at zero frequency and second harmonic frequency of the laser, but inaccuracy of the dispersion relation at these frequencies makes dubious the physical realization of these instabilities, which have approximately millisecond growth times.

Calculations have been made of the focusing distance and intensification of a self-focused high-power laser beam. Self-focusing is due to an increase of the index of refraction of the propagation medium which is proportional to the local laser intensity. Computer solutions were obtained from an approximate nonlinear wave equation, which is valid when the intensity varies slowly over a wavelength, for an input beam with a plane wavefront and a Gaussian radial intensity profile. Typically, a 1-MW beam of 2-mm diameter would focus itself in about 50 cm of  $\text{CS}_2$ .

Dielectric breakdown in water produced by a focused Q-switched ruby laser resulted in an unexplained blue emission with wavelengths ranging from 3200 to 4500 Å, with a minimum at 3600 Å. The emission lasted 20 nsec or less, aside from a long but weak afterglow.

Fluorescence from limonene, possibly produced by multiple-photon absorption from a plane-polarized ruby laser beam, showed little depolarization due to Brownian rotation of the excited molecules during their radiative lifetime. Considering the value of the rotation relaxation time, one estimates that the radiative lifetime is less than 0.1 nsec, which is consistent with direct measurements of the fluorescent decay.

Analysis of the symmetry of molecular polarizability tensors shows that no incoherent emission of sum frequency light will arise from density fluctuations unless the medium is optically active and unless the two primary frequencies are different; otherwise, the sum frequency emission may arise from orientation fluctuations.

Stimulated Stokes and anti-Stokes lines have been obtained in quartz, using a high-power ruby laser as a source. As part of an investigation of the interference between Brillouin and Raman effects in solids, details of the spectrum have been compared with spontaneous Raman scattering in quartz.

The Bose-Einstein distribution has been confirmed for the photoelectron counts from a photomultiplier which is illuminated by a gas laser operating just below threshold, as expected for a narrow-band Gaussian source when the counting interval is less than the inverse bandwidth of the light.

### III. MATERIALS RESEARCH

Liquidus temperatures for the portions of the Hg-Te system from 3 to 25 and from 50 to 100 atomic-percent tellurium have been determined by differential thermal analysis. These results have been combined with liquidus points obtained earlier from partial pressure data to establish the Hg-Te phase diagram.

The pressures of mercury and selenium in the vapor over Hg-saturated, Se-saturated, and congruently subliming HgSe(c) between 450° and 800°C have been determined by measuring the optical absorption of the vapor. The pressure data have been used to obtain the first reported values for the standard Gibbs free energy of formation of HgSe(c).

At sufficiently low temperatures, the high-pressure phase of InTe can be retained at atmospheric pressure as a metastable phase. The heat evolved when this metastable phase is transformed at atmospheric pressure into the stable low-pressure form has been measured by both metal-solution and differential-scanning calorimetry. The heat of transformation is 0.44 kcal/g-atom.

High-pressure phases can also be retained at atmospheric pressure in  $\text{InSb(II)}_{1-x}(\text{2 In})_x$  samples kept at sufficiently low temperatures. Qualitative results on the amount of heat liberated when such samples are transformed at atmospheric pressure indicate the existence of a high-pressure phase different in structure from either InSb(II) or indium. This phase lies between  $x = 0.17$  and  $x = 0.60$ , but its exact composition has not been determined.

The temperature at which the phase of MnAs with B8 structure is transformed into the high-temperature B31 form has been measured as a function of hydrostatic pressure. The transition temperature decreases from 44°C at atmospheric pressure to -72°C at 4.5 kbar. The functional dependence of transition temperature on pressure indicates that the B31 phase is stable at all temperatures for pressures exceeding 4.5 kbar.

Electrical measurements have been made on  $\text{Ti}_2\text{O}_3$  single crystals containing considerably less nitrogen, the principal impurity, than earlier samples. In contrast to previous results, both resistivity and Hall coefficient depend strongly on orientation. The magnetoresistance,  $\Delta\rho/\rho_0$ , is 2.5 at 4.2°K and 170 kG, compared with the previous maximum value of 0.12.

The concept of a Jahn-Teller theorem for narrow-band electrons has been formalized and applied to the interpretation of the localized vs collective character of outer d-electrons in a wide range of transition-metal compounds.

Wet chemical methods have been developed for determining cobalt and the rare earth element in the lanthanum and yttrium cobalt oxides, and for determining all three major components in iron-nickel-copper thin films.

#### IV. PHYSICS OF SOLIDS

Reflectivity measurements in  $\text{ReO}_3$ , which were previously reported in the range from 0.2 to 3.8 eV, have now been extended to 12 eV. Results indicate a Drude-like behavior in the energy region below 2 eV and peaks at 4.6 and 9.6 eV arising from interband transitions. A Kramers-Kronig analysis of the reflectivity has been used to obtain the real and imaginary parts of the dielectric constant, and a further separation of the dielectric constant components into free-electron and interband contributions has been made.

Concurrently, a tight binding scheme is being used to investigate the electronic band structure of  $\text{ReO}_3$ . The energy levels have been found to separate into  $\sigma$  and  $\pi$  bonding and antibonding bands, and into a set of nonbonding  $\pi$  bands. Estimates of the various parameters are being made, using the augmented plane-wave method to calculate the energy values at the high symmetry points of the Brillouin zone. This calculation will be used to predict optical, magnetic, and transport properties.

Experimental investigation of the band structure of GaSe is continuing. A reduced effective mass  $m^* = 0.14m$  and an energy gap  $\epsilon_g = 2.130$  eV have been obtained from more highly resolved oscillatory magnetoabsorption data at 1.5°K in the Faraday configuration. The data in the Voigt configuration are smaller in amplitude and more complex, suggesting that more than one transition is involved. In the zero-field data, three clearly defined exciton peaks have been resolved; these have been used to calculate a binding energy of 21 meV and a reduced effective mass  $m^* = 0.17m$ , which is consistent with the results of the magneto-optical data. Several models for GaSe which are consistent with the experimental data have been proposed.

GaSe is also being examined in the microwave region at 70 GHz in order to observe intraband cyclotron resonance. So far, a well-resolved magnetoabsorption peak corresponding to an effective mass  $m^* = 0.02m$  and an  $\omega\tau \sim 1.5$  has been observed, but only in one sample.

Another microwave resonance experiment, on p-type PbSe, is continuing. Marked structure has been obtained below 3 kG and identified with dielectric anomalies; this behavior is consistent with that predicted on the basis of a classical skin effect theory, using an infinite relaxation time and values of effective mass and anisotropy obtained from previous Shubnikov-de Haas measurements on the same sample.

A new approach to the tight-binding technique for phenomenologically obtaining the energy bands in solids has been developed. This method involves a Fourier expansion for the energy bands in k-space in which the symmetry of the lattice and the degeneracies of the bands at high symmetry points are included. The Fourier coefficients of the expansion are evaluated from experimentally observed parameters. This approach is being tested on the metal, aluminum, and the semimetal, antimony.

An electron-beam technique has been developed for the vapor deposition of piezoelectric semi-insulating CdS thin films on various substrates. By proper orientation of the electric field, either longitudinal or transverse hypersonic waves can be excited. Acoustically active films have been deposited on metals, semiconductors, and insulators; pulse-echo techniques have been used to test the acoustical activity of a film. The range of frequency excitation in the longitudinal mode for active films varied from 12.4 MHz for thick films deposited on aluminum to 70 GHz for thin films deposited on a z-cut quartz rod.

The study of the magnetic properties of the spinels  $ACr_2X_4$ , where A is nonmagnetic zinc or cadmium and X is oxygen, sulfur, or selenium, is continuing. Magnetic measurements on  $CdCr_2O_4$ , an antiferromagnet with a Néel temperature  $T_N = 9^\circ K$ , have been completed;  $CdCr_2S_4$  has been found to be ferromagnetic with a Curie temperature  $T_C = 86^\circ K$ . It has been found that, in addition to the large dependence on lattice size for a given type of A-site ion,  $T_A$ , the asymptotic Curie temperature, in this entire series of compounds depends strongly on whether the A-site ion is zinc or cadmium. Since  $T_A$  is proportional to the sum of all magnetic exchange interactions, this indicates that the diamagnetic A-site cation significantly affects these interactions. Specifically, substituting zinc for cadmium tends to decrease the ferromagnetic nearest-neighbor interaction, or to increase the antiferromagnetic next-nearest-neighbor interaction, or both.

In order to resolve inconsistencies in  $MnCr_2O_4$  between the nuclear magnetic resonance and neutron diffraction results for the manganese cone angle, these properties were reinvestigated. The new data are in general agreement with the earlier findings, but indicate that the  $Mn^{++}$  ions possess a reduced magnetic moment of about  $4.3\mu_\beta$ , rather than the previously assumed value of  $5.0\mu_\beta$ . However, while use of this reduced moment improves the agreement between the theoretical and experimental neutron diffraction patterns, the discrepancy with the nuclear magnetic resonance result remains.

An experimental study of the temperature variation of the spin wave dispersion relation  $\epsilon_k = Dk^2 - Fk^4$  has indicated that for a 63%Ni-37%Fe film 6950 Å thick, both the quartic and the quadratic coefficients vary as  $T^{5/2}$  up to  $80^\circ K$  and approximately as  $T^{3/2}$  up to  $298^\circ K$ . A theoretical justification for the temperature dependence of D and F in the spin wave dispersion relation can be simply made by extending a model proposed by W. Marshall for treating a system of interacting spins which gave the  $T^{5/2}$  dependence of D. Higher-order terms occurring in D, as well as the temperature dependence of F, predict a  $T^{5/2}$  dependence for F, a higher-order  $T^{7/2}$  term for D, and a relation between the three temperature coefficients of D and F.

An expression has been derived that relates the fluctuation scattering of light expected from a ferromagnet to the observed Faraday- or Kerr-effect coefficient and to the spin-spin correlation function. An estimate is made of the fluctuation scattering to be anticipated near the Curie temperature.

Experimental methods of observing zero sound modes in metals are considered. It is concluded that a mode characterized by a paramagnetic spin wave is likeliest to exist, and should most readily be observed in metals which show superconductivity. It is argued that these zero sound modes may exist in the superconducting state as well.

A simple and general argument has been found for considering pseudomomentum for an ensemble of interacting phonons. It is shown that the anticipated selection rule on pseudomomentum holds for any process produced by phonon-phonon interaction.

The energy spectrum of a polaron has been considered in the region where its excitation energy is close to that of an optical phonon. Both a variational and weak coupling calculation, which are consistent with each other, have been performed. It is found that the dispersion relation in the weak coupling theory becomes flat as the polaron momentum approaches the value at which the polaron excitation energy and the optical phonon energy become equal.

A treatment has been formulated of the kinetic equation for a system of electrons under the action of arbitrary space- and time-varying fields and a random distribution of impurities. The results can be used to derive a Boltzmann equation for the system. Kinetic equations for other situations, including the presence of a quantizing magnetic field, can be readily obtained.

The interaction of photons with charged particles in a plasma modifies the dispersion relation for electromagnetic propagation in a well-known way. It is shown that this result can be obtained quite simply from quantized field theory, and that it arises because of the  $\vec{A}^2$  term in the electromagnetic energy, averaged over the charged particles of the medium.

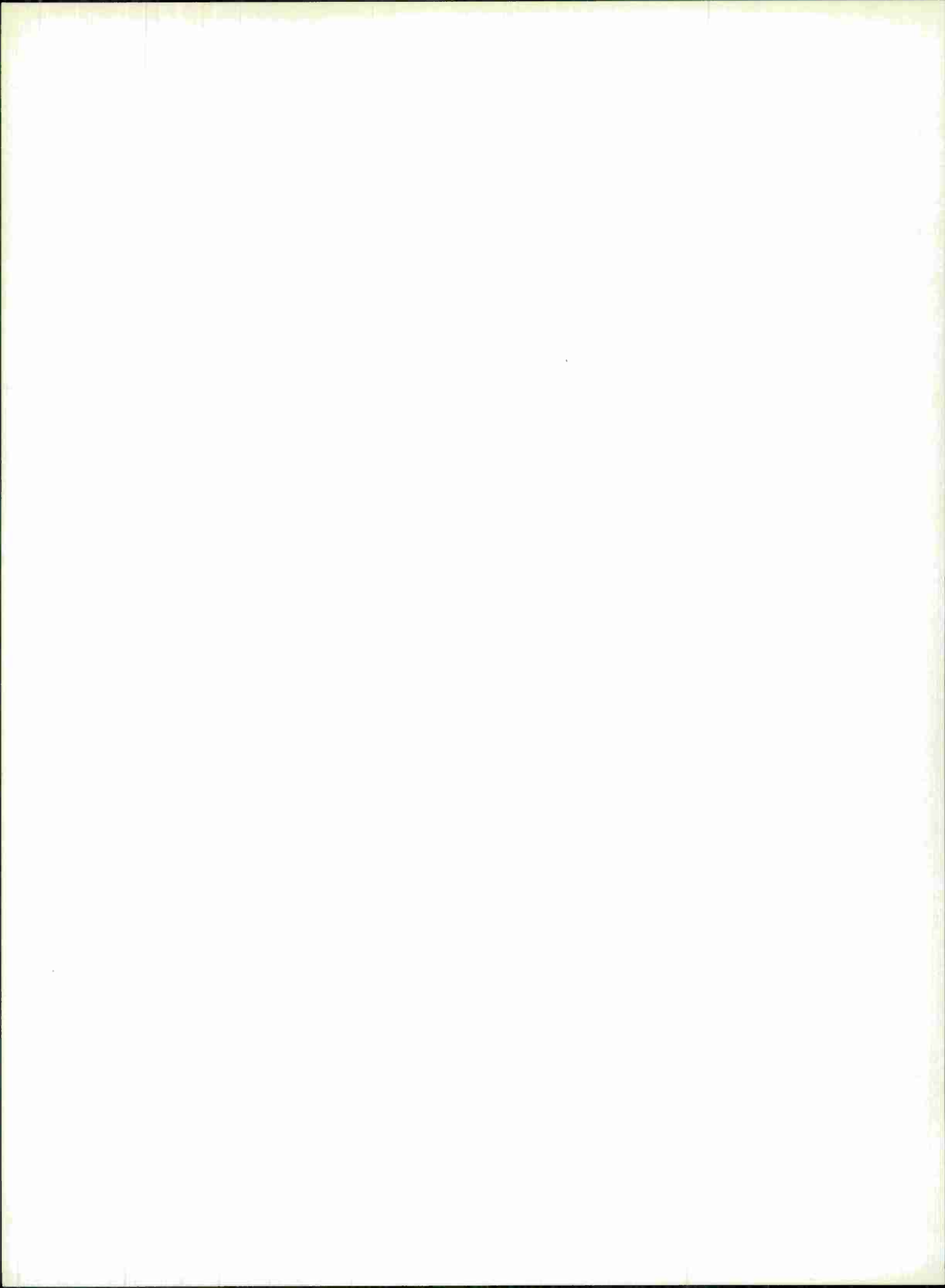


# TABLE OF CONTENTS

Abstract	iii
Introduction	iv
Organization	xiii
Reports by Authors Engaged in Solid State Research	xiv
I. SOLID STATE DEVICE RESEARCH	1
A. Extension of Pressure Tuning of PbSe Diode Laser to 22 $\mu$	1
B. Solution Regrowth of Planar InSb Laser Structures	1
1. Introduction	1
2. Method and Results	2
3. Discussion	3
C. Injection Mechanisms in InSb $n^+pp^+$ Structures	5
1. Experimental Technique	5
2. Low Current Range	6
3. High Current Range	9
D. Bulk GaAs Microwave Amplifiers	9
II. LASER RESEARCH	15
A. Nonconvective Instabilities in Raman Media	15
B. Self-Focusing of Optical Beams	15
C. High Power Laser Effects in Liquids	17
D. High Power Brillouin and Raman Scattering in Solids	18
E. Photoelectron Statistics Produced by Laser Operating Below Threshold of Oscillation	19
III. MATERIALS RESEARCH	25
A. Hg-Te Phase Diagram	25
B. Pressures of Hg and Se in Equilibrium with HgSe(c)	26
C. Thermodynamic Studies of InTe Pressure-Temperature Diagram	27
D. High-Pressure InSb-In System	31
E. Pressure Dependence of $B8 \rightleftharpoons B31$ Transition Temperature in MnAs	31
F. Electrical Properties of $Ti_2O_3$	33
G. Theory: Localized vs Collective Electrons in Transition-Metal Compounds	33
H. Wet Chemical Analysis	33
1. Lanthanum and Yttrium Cobalt Oxides	33
2. Iron-Nickel-Copper Alloy Thin Films	34

IV. PHYSICS OF SOLIDS	37
A. Electronic Band Structure	37
1. Reflectivity of $\text{ReO}_3$	37
2. Band Structure of $\text{ReO}_3$	38
3. Magnetoabsorption of Direct Transition in Gallium Selenide	38
4. Cyclotron Resonance in Gallium Selenide	41
5. Magnetoplasma Cyclotron Resonance in p-Type Lead Selenide	42
6. Fourier Expansion for Energy Bands in a Periodic Solid	42
B. Hypersonic Waves in Solids	43
1. Generation of Hypersonic Waves by Using Thin-Film CdS Transducers	43
2. Microwave Phonon Generation	45
C. Magnetism	45
1. Magnetic Properties of Chromium Spinel with Nonmagnetic A-Sites	45
2. Reduced Manganese Moment in Manganese Chromite	46
3. Temperature Variation of Spin Wave Dispersion Relation	46
4. On Marshall's General Spin Wave Theory	47
5. Light Scattering from Spin Fluctuations in Ferromagnets	48
6. Paramagnetic Spin Waves in Superconductors	49
D. Quantum Transport Theory	50
1. Pseudomomentum of Phonons	50
2. Polaron Energy Spectrum	51
3. Quantum Theory of Kinetic Equations for Electrons in Random Impurities	51
4. Quasi-Photons in Charged Media	52

# ORGANIZATION

## SOLID STATE DIVISION

A. L. McWhorter, *Head*  
P. E. Tannenwald, *Associate Head*  
M. J. Hudson, *Assistant*  
E. P. Warekois  
D. T. Stevenson\*  
T. C. Harman†

## SOLID STATE THEORY

H. J. Zeiger, *Leader*  
M. M. Litvak, *Assistant Leader*

Argyres, P. N.	Mason, V. J.
Dresselhaus, G. F.	Mason, W. C.
Houghton, B. H.*	Rawson, N. B.*
Kaplan, T. A.	Stanley, H. E.*
Kelley, P. L.	Trent, P. H.
Kleiner, W. H.	Van Zandt, L. L.
Larsen, D. M.	

## OPTICS AND INFRARED

R. H. Kingston, *Leader*  
R. J. Keyes, *Assistant Leader*

Bates, D. H.	Longaker, P. R.
Bostick, H. A.	McGowan, J.
Carbone, R. J.	Walters, E.
Dennis, J. H.	Zimmerman, M. D.
Freed, C.	

## ELECTRONIC MATERIALS

J. B. Goodenough, *Leader*  
J. M. Honig, *Associate Leader*  
A. J. Strauss, *Assistant Leader*

Andrews, H. I.‡	Kafalas, J. A.
Arnott, R. J.	LaFleur, W. J.
Bachner, F. J.‡	Lavine, M. C.*
Banus, M. D.	Newman, W. A.
Brebrick, R. F.	O'Connor, J. R.
Button, M. J.	Owens, E. B.
Cornwell, J. C.	Paladino, A. E.
Delaney, E. J.	Plonko, M. C.
Ehlers, H. H.	Pollard, E. E.‡
Fahey, R. E.	Rabbio, M. A.
Farrell, L. B.	Raccach, P. M.
Ferretti, A.	Reed, T. B.†
Finn, M. C.	Ridgley, D. H.
Fischler, S.	Roddy, J. T.
Germann, R. W.	Siuta, V. P.‡
Hilsenrath, S.	Sohn, J. B.

## SOLID STATE PHYSICS

J. G. Mavroides, *Leader*  
G. B. Wright, *Assistant Leader*

Bermon, S.	Kolesar, D. F.
Burke, J. W.	Krag, W. E.
Carman, R. L.*	Mastromattei, E. L.
Dickey, D. H.	Menyuk, N.
Dresselhaus, M. S.	Parker, C. D.
Dwight, K., Jr.	Perry, F. H.
Feinleib, J.	Schlossberg, H. R.‡
Feldman, B.	Scouler, W. J.
Fulton, M. J.	Stickler, J. J.‡
Groves, S. H.	Strahm, N. D.‡
Halpern, J.	Thaxter, J. B.
Johnson, E. J.	Weber, R.
Kernan, W. C.	Weinberg, D. L.

## APPLIED PHYSICS

R. H. Rediker, *Leader*  
J. O. Dimmock, *Assistant Leader*

Butler, J. F.	MeIngailis, I.
Calawa, A. R.	Mooradian, A.
Carter, F. B.	Nill, K. W.
Caswell, F. H.	Palermo, J. S.
Clough, T. F.	Phelan, R. J., Jr.
Donaldson, P. L.	Quist, T. M.
Foyt, A. G., Jr.	Sullivan, F. M.
Grant, C. R.	Walpole, J. N.
Hinkley, E. D.	Ward, J. H. R., III
Hurwitz, C. E.	Wolfe, C. M.
Lindley, W. T.	Womac, J.
McPhie, J. M.	Youtz, P.

\* Part Time

† Leave of Absence

‡ Research Assistant

# REPORTS BY AUTHORS ENGAGED IN SOLID STATE RESEARCH

15 August through 15 November 1965

## PUBLISHED REPORTS

TR No.	<u>Technical Report</u>	<u>DDC Nos.</u>
390	Elements of the Hijmans-de Boer Approximation to Order-Disorder Theory  J. M. Honig	26 May 1965  DDC*
<u>Journal Articles†</u>		
JA No.		
2495	The Effect of Trivalent Manganese on the Crystal Symmetry of Some Lithium Spinel  D. B. Rogers R. W. Germann R. J. Arnott	J. Appl. Phys. <u>36</u> , 2338 (1965), DDC 622323
2516	Chemical Inhomogeneities and Square B-H Loops  J. B. Goodenough	J. Appl. Phys. <u>36</u> , 2342 (1965), DDC 622927
2523	Field Effect on Magnetoresistance of n-Type Indium Antimonide  S. Kawaji‡ H. Huff‡ H. C. Gatos	Surface Sci. <u>3</u> , 234 (1965)
2530	Preparation and Paramagnetism of the Rare Earth Trifluorides  S. Kern P. M. Raccach	J. Phys. Chem. Solids <u>26</u> , 1625 (1965)
2550	Spin-Orbit Interaction in Graphite  G. F. Dresselhaus M. S. Dresselhaus	Phys. Rev. <u>140</u> , A401 (1965)
2556	Long-Range Exchange Interactions from Spin-Wave Resonance  R. Weber P. E. Tannenwald	Phys. Rev. <u>140</u> , A498 (1965)
2579	Impurity and Exciton Effects on the Infrared Absorption Edges of III-V Compounds  E. J. Johnson H. Y. Fan‡	Phys. Rev. <u>139</u> , A1991 (1965)
2588	Quenching of Dy <sup>+2</sup> Fluorescence by Y <sup>+2</sup> in CaF <sub>2</sub> :Dy <sup>+2</sup> Lasers  J. R. O'Connor	Appl. Phys. Letters <u>7</u> , 54 (1965)

\* Not yet assigned.

† Reprints available.

‡ Author not at Lincoln Laboratory.

Published Journal Articles (Continued)

JA No.			
2589	Effect of $Y^{+3}$ on the Reduction of $Sm^{+3}$ in $CaF_2$	J. R. O'Connor R. M. Hilton	Appl. Phys. Letters <u>7</u> , 53 (1965)
2590	Simple Apparatus for Applying Uniaxial Pressure at Very Low Temperatures	J. H. R. Ward	Rev. Sci. Instr. <u>36</u> , 1376 (1965)
2604	PbS Diode Laser	J. F. Butler A. R. Calawa	J. Electrochem. Soc. <u>112</u> , 1056 (1965)
2629	Physics of Quantum Electronics - A Conference Report	P. E. Tannenwald P. L. Kelley B. Lax	Phys. Today <u>18</u> , No. 9, 58 (1965)
2636	Pressure-Tuned PbSe Diode Laser	J. M. Besson* J. F. Butler A. R. Calawa W. Paul* R. H. Rediker	Appl. Phys. Letters <u>7</u> , 206 (1965)
2638	Absolute Instabilities with Drifted Helicons	A. Bers* A. L. McWhorter	Phys. Rev. Letters <u>15</u> , 755 (1965)
MS No.			
1383	Electrical and Electro-Optical Properties of GaAs-InSb "Schottky" Heterojunctions (Abstract)	E. D. Hinkley R. H. Rediker	IEEE Trans. Electron Devices <u>ED-12</u> , 511 (1965)
1384	Transients and Hot Carrier Effects in InSb Bulk Injection Lasers (Abstract)	I. Melngailis	IEEE Trans. Electron Devices <u>ED-12</u> , 506 (1965)
1385	Properties of Optically Pumped Semiconductor Lasers (Abstract)	R. J. Phelan, Jr.	IEEE Trans. Electron Devices <u>ED-12</u> , 506 (1965)

\* \* \* \* \*

UNPUBLISHED REPORTS

Journal Articles

JA No.			
2591	Properties of InAs Lasers	I. Melngailis R. H. Rediker	Accepted by J. Appl. Phys.
2609	deHaas-van Alphen Effect in Pyrolytic and Single Crystal Graphite	S. J. Williamson* S. Foner* M. S. Dresselhaus	Accepted by Phys. Rev.

---

\* Author not at Lincoln Laboratory.

Unpublished Journal Articles (Continued)

JA No.			
2610	Pressures of Hg and Selenium over HgSe(c) from Optical Density Measurements	R. F. Brebrick	Accepted by J. Chem. Phys.
2621	Superconductivity in the Transition Metal Carbides: Mo <sub>4.8</sub> Si <sub>3</sub> C <sub>0.6</sub> , Mo <sub>0.95</sub> Hf <sub>0.05</sub> C <sub>0.75</sub> and Mo <sub>2</sub> C	V. Sadagopan* H. C. Gatos	Accepted by J. Phys. Chem. Solids
2622	Towards a Theory of the Anomalous Thermoelectric Effect in Magnetically Dilute Alloys	L. L. Van Zandt A. W. Overhauser*	Accepted by Phys. Rev.
2626	Photocurrent Spectrum and Photoelectron Counts Produced by a Gaseous Laser	C. Freed H. A. Haus*	Accepted by Phys. Rev.
2633	A Note Concerning the Temperature Profile Within a Thermomagnetic Energy Converter	T. C. Harman J. M. Honig	Accepted by Adv. Energy Conversion
2637	Non-Stoichiometry in Binary Semiconductor Compounds, $M_{\frac{1}{2}-\delta}N_{\frac{1}{2}+\delta}(c)$	R. F. Brebrick	Accepted as chapter in <u>Progress in Chemistry of the Solid State</u> , Vol. 3 (Pergamon Press, New York)
2641	Magnetic and Electric Properties of ReO <sub>2</sub> : Theoretical Interpretations	J. B. Goodenough P. Gibart* J. Brenet*	Accepted by Compt. rend.
2642	Solution Regrowth of Planar InSb Laser Structures	I. Melngailis A. R. Calawa	Accepted by J. Electrochem. Soc.
2644	The Gunn Effect in Polar Semiconductors	A. G. Foyt A. L. McWhorter	Accepted by IEEE Trans. Electron Devices
2653	Resistance-Heated Crystal Puller for Operation at 2000°C	T. B. Reed R. E. Fahey	Accepted by Rev. Sci. Instr.
2697	Bulk GaAs Microwave Amplifiers	A. G. Foyt T. M. Quist	Accepted by IEEE Trans. Electron Devices

Meeting Speeches†

MS No.			
1374	Semiconductor Lasers	R. H. Rediker	} Symposium on Materials Science and Engineering, M.I.T., 30 September 1965
1377	Surface Characteristics of Compound Semiconductors	H. C. Gatos	

\* Author not at Lincoln Laboratory.

† Titles of Meeting Speeches are listed for information only. No copies are available for distribution.

Unpublished Meeting Speeches (Continued)

MS No.			
1394A	Magneto-Optical Effects in Solids	G. F. Dresselhaus	Seminar, Ford Scientific Laboratory, Dearborn, Michigan, 25 October 1965
1419	Influence of Metal-Metal Bonding on Structures Derived from the NiAs Structure	J. B. Goodenough	CIC Symposium, Dalhousie University, Halifax, Canada, 1-3 September 1965
1431	Atomistic Approach to Electronic Materials	H. C. Gatos	NATO Summer School, Salonica, Greece, 16-20 August 1965
1438	Optical Properties of Rare-Earth Metals	A. J. Freeman* J. O. Dimmock R. E. Watson*	} International Colloquium on Optical Properties and Electronic Structure of Metals and Alloys, Paris, 13-16 September 1965
1451	Magnetoreflexion Studies in the Band Structure of Antimony	M. S. Dresselhaus J. G. Mavroides	
1447	Semiconductor Bulk Injection Lasers	I. Melngailis	NEREM, Boston, 3-5 November 1965
1460	Application of Magneto-Optical Phenomena	M. S. Dresselhaus	IEEE, French Section, Paris, 14 September 1965
1461	Color Centers in Alkaline Earth Fluorides	J. H. Chen* J. R. O'Connor	} International Conference on Color Centers, University of Illinois, 11-13 October 1965
1462	Thermoluminescence and Dynamical Jahn-Teller Effects in Irradiated CaF <sub>2</sub> (Y)	J. R. O'Connor J. H. Chen*	
1475A	A Covalency Criterion for Ligand-Field vs Band Electrons in Oxides with the Perovskite Structure	J. B. Goodenough	Seminar, Tufts University, 27 October 1965
1481	Description of Transition-Metal Compounds: Application to Several Sulfides	J. B. Goodenough	Colloque International sur les Derives Semi-metalliques, University of Paris, 27 September - 1 October 1965
1482	Principles of Lasers	I. Melngailis	Latvian League of Boston, Boston, 25 September 1965
1488	A Structural Criterion for Band vs Localized d Electrons	J. B. Goodenough	Seminar, University of Bordeaux, 5-6 October 1965
1492	The Gunn Effect in Polar Semiconductors	A. L. McWhorter	1965 Electron Devices Meeting, Washington, D. C., 20-22 October 1965

---

\* Author not at Lincoln Laboratory.

Unpublished Meeting Speeches (Continued)

MS No.			
1492A	Transferred Electron Effects in Polar Semiconductors	A. G. Foyt	Seminar, Naval Ordnance Labora- tory, Silver Spring, Maryland, 4 November 1965
1497	Time Inversion and Transport Coefficients for Magnetic Crystals	W. H. Kleiner	} American Physical Society, Chicago, Illinois, 29 October 1965
1499	Excitation Spectra of Group III Impurities in Germanium Under Uniaxial Stress	D. H. Dickey J. O. Dimmock	
1522	Evidence for Impurity States Associated with High Energy Conduction Band Extrema in n-CdTe	A. G. Foyt R. E. Halsted* W. Paul*	
1509	Electrical Properties of Metal Oxides	J. M. Honig	Seminar, Purdue University, 27 October 1965
1511	Deviations from Stoichiometry in Electronic Materials	A. J. Strauss	Seminar, Tyco Laboratories, Inc., Waltham, Massachusetts, 20 Octo- ber 1965
1517	The Symmetry of Hartree-Fock Ground States	W. H. Kleiner	Seminar, Monsanto Company, St. Louis, Missouri, 27 October 1965
1520	Self-Focusing of Optical Beams	P. L. Kelley	Seminar, M.I.T., 29 October 1965
1521	Determination of Band Structure of GaSe from Magneto-Optical Absorption Experiments	J. Halpern	Seminar, National Magnet Labora- tory, M.I.T., 27 October 1965

---

\* Author not at Lincoln Laboratory.

## I. SOLID STATE DEVICE RESEARCH

### A. EXTENSION OF PRESSURE TUNING OF PbSe DIODE LASER TO 22 $\mu$ \*

The measurements reported in the previous Solid State Research Report (1965:2) have been extended to higher pressures with the development of windows made of high-resistivity polycrystalline germanium or silicon formed in the shape of cylinders 12 mm diameter by 12 mm long. The ends of the cylinders were optically polished. One end was placed over a 3-mm hole in the pressure vessel. Under these conditions all windows tested held to 20 kbar with no evidence of deterioration. Germanium windows were used for wavelengths to 20  $\mu$  in order to eliminate transmission difficulties due to lattice absorption bands in silicon between 8 and 20  $\mu$ ; silicon windows were used for wavelengths above 20  $\mu$ , where germanium has lattice absorption bands.

Development of these windows has made possible an extension of the experiments to the freezing pressure of helium at 77°K, which was found to be  $14.15 \pm 0.03$  kbar. The corresponding diode emission wavelength was 22  $\mu$ . Pressure tuning of the PbSe diode emission wavelength from 7.5 to 22  $\mu$  is shown in Fig. I-1. As the helium freezes, the rate of change in the wavelength of the emission with applied pressure decreases abruptly, making possible an accurate determination of the freezing pressure of helium. Since the pressure cannot be transmitted reliably through the solid helium, we plan to extend the diode emission to longer wavelengths by pressurizing the system to above 14 kbar at room temperature (where helium is still a gas), and then cooling it to 77°K and below. Also, in our preliminary experiment, once the helium froze, the diode laser emission decreased to the point where it was barely discernible. Since the emission intensity returned to its original value each time the pressure was reduced below the helium freezing pressure, the diode suffered no permanent physical damage in the process. The emission intensity decrease is believed to be due to scattering of the radiation by the solid helium. To minimize scattering, the diode package has been modified so that the diode emitting edge can be placed within 0.05 mm of the window surface.

J. M. Besson<sup>†</sup>  
A. R. Calawa  
W. Paul<sup>†</sup>

### B. SOLUTION REGROWTH OF PLANAR InSb LASER STRUCTURES

#### 1. Introduction

The growth of thin crystal layers from a melt was first used by Nelson<sup>1</sup> as a technique of producing remarkably flat and abrupt p-n junctions for germanium tunnel diodes and GaAs junction lasers. In the case of InSb, this process is of particular interest for growing an n-type layer on a p-type substrate, because of the difficulty of producing such layers by diffusion. Diffusion of n-type impurities such as selenium, tellurium, or sulfur is impractical because these elements tend to form glass-like compounds on the substrate surface, and their diffusion coefficients in InSb are small at temperatures below the melting point of InSb (525°C). By the

\* The work described in this section was supported in part by the AF Avionics Laboratory Director's Fund, Item Nr. 65-86.

<sup>†</sup> Harvard University.

Section I

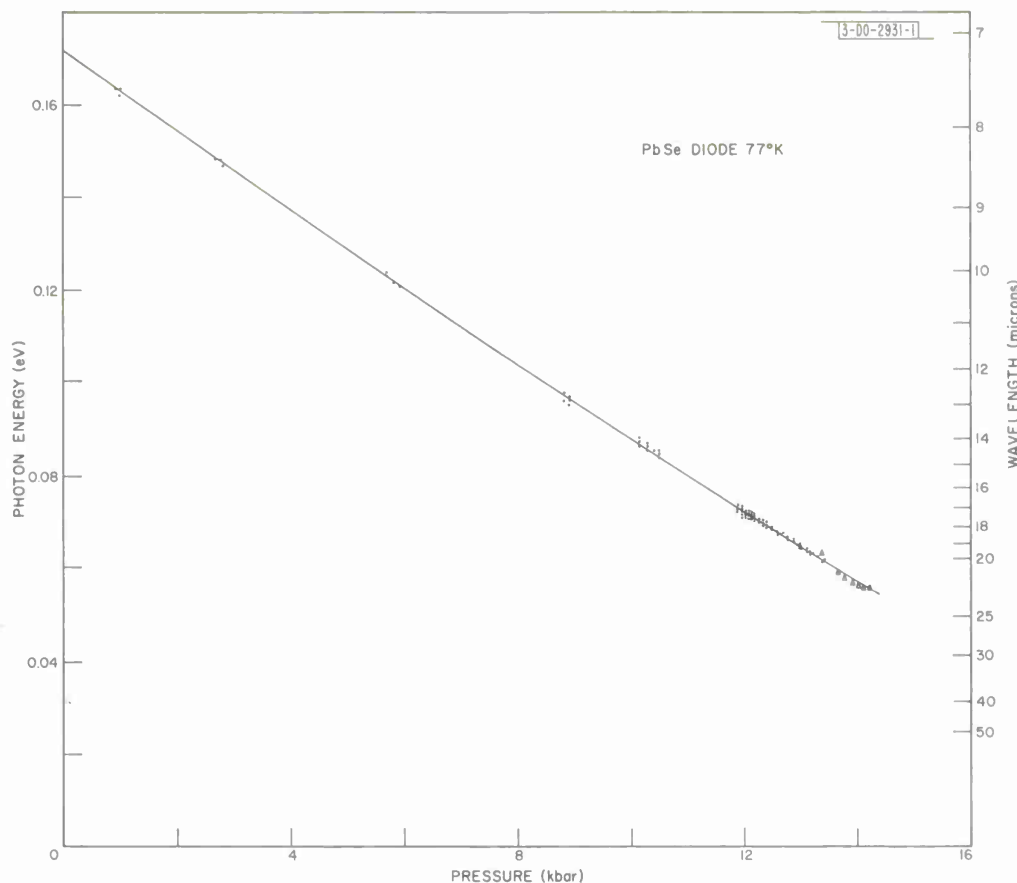


Fig. I-1. Variation with pressure of dominant emission modes from PbSe diode laser at 77°K.

solution-regrowth technique, an n-type layer can be grown easily on a p-type substrate by simply adding an n-type dopant, such as tellurium, to the melt.

## 2. Method and Results

As shown in Figs. I-2(a-b), the apparatus consists of a boron-nitride container which is heated from the bottom by passing current through a graphite heater strip and which can be tilted at various times during a run. One side of the boat contains the InSb substrate, while the opposite side contains indium and a sufficient amount of InSb to produce a nearly saturated In-InSb solution at the maximum temperature of about 300°C. When n-type layers are grown, a small amount of tellurium is added to the solution. The melt and the substrate are kept apart during the first part of the run by a small ridge in the bottom of the boat. Molten stearic acid is then poured into the boat to cover the substrate and the melt. The purpose of the stearic acid is to keep the surface of the substrate and of the melt clean and to insure good uniform wetting of the substrate surface by the melt. The boat is then heated by the graphite heater strip. At about 300°C the boat is tilted so that the melt flows over the substrate, and the current in the heater is reduced immediately to begin cooling the boat. When the melt first makes contact with the substrate, the melt is not quite saturated with InSb and a thin layer of the substrate

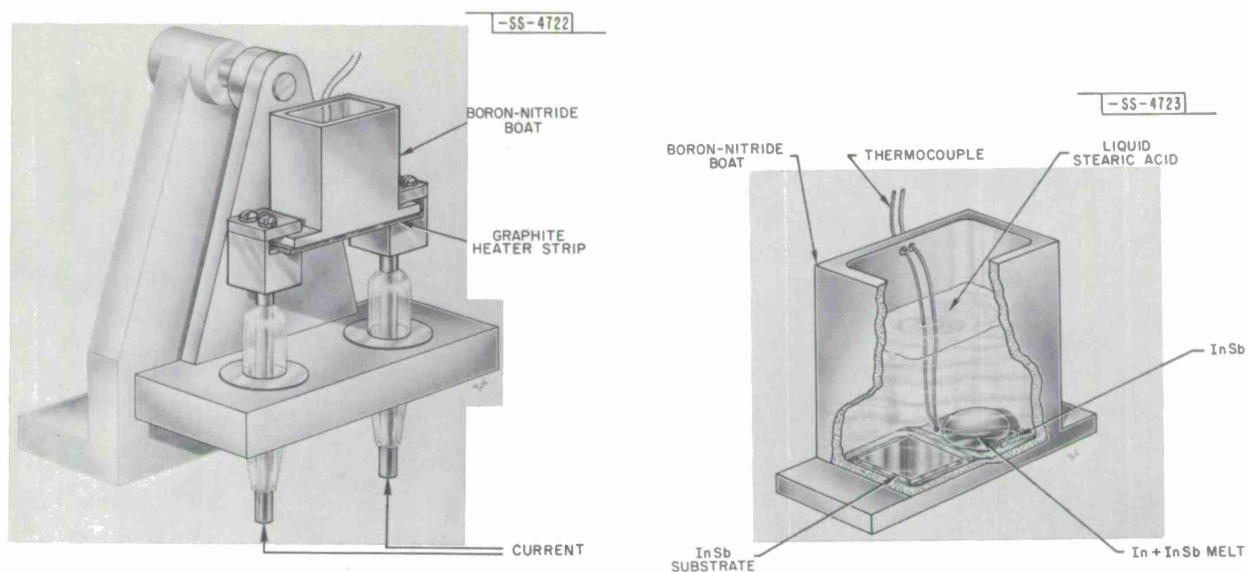


Fig. I-2. (a) Apparatus for solution regrowth showing mount for boron-nitride boat.  
(b) Inside view of boron-nitride boat.

surface goes into solution. This removes any surface damage. As the temperature is lowered, InSb is forced out of the solution and grows in a uniform layer on top of the substrate. At about 200° to 250°C the boat is tilted back and the remaining solution is wiped off the substrate. The stearic acid is then poured off before it solidifies. The grown surface generally has a clean mirror-like appearance and the growth is quite uniform across the substrate. Figures I-3(a-b) show the profile of a grown junction delineated by etching a cleaved (110) surface. All our solution regrowths were done on a (100) crystal face to enable cleaving perpendicular to the junction plane.

The weights of the various ingredients of the melt used in growing a heavily doped  $n^+$  region on a p-type substrate area of  $12 \times 12$  mm were 4.0 g of indium, 0.6 g of n-type InSb, and 4.0 mg of tellurium. The weight of the tellurium dopant in this case was chosen to produce the highest possible doping in the  $n^+$  layer ( $8 \times 10^{18}/\text{cm}^3$ ).<sup>2,3</sup> The ratio of the InSb weight to the weight of indium in the melt was chosen from published solubility data.<sup>4</sup> Figure I-4 is the temperature variation of the fractional weight of InSb required to produce a saturated solution.

A typical heating cycle is shown in Fig. I-5. The melt is poured over the substrate by tilting the boat at the maximum temperature of 315°C in this case. At about 225°C the melt is wiped off. Although most of our runs were similar to this one, the times and temperatures involved do not appear to be critical.

### 3. Discussion

The main innovation of our solution-regrowth technique is the use of stearic acid, which facilitates growing at the low temperatures required for InSb. Using a liquid instead of a gas atmosphere also greatly simplifies the apparatus and the process, and permits visual observation during the process. Although the use of stearic acid is limited to temperatures not higher than 350°C, at which point it boils away too rapidly, other liquids such as boric oxide could be used for crystals which require higher growth temperatures than InSb.

-85-4058

-85-4059

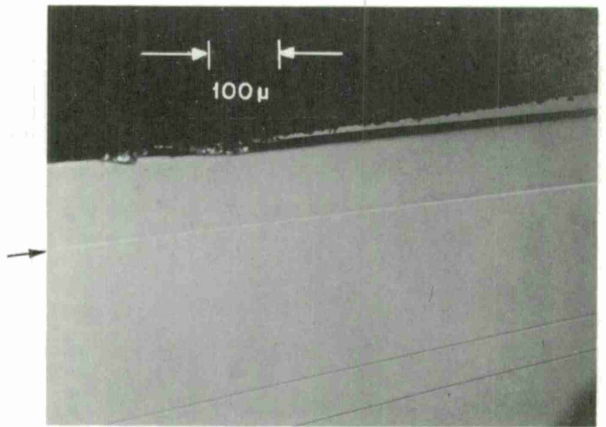
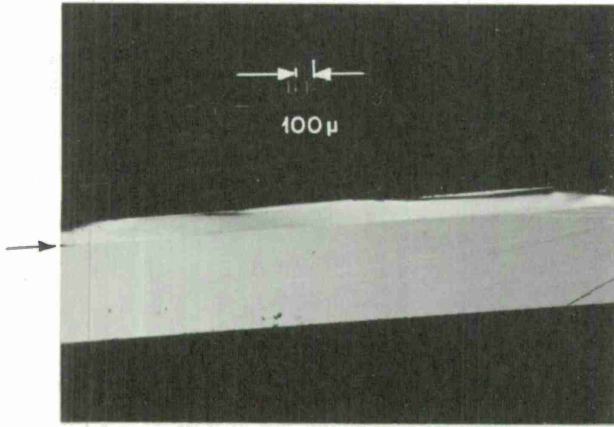


Fig. I-3. (a) Profile of 120- $\mu$ -thick  $n^+$  layer grown on (100) face of p-type InSb substrate. Junction indicated by arrow has been delineated by etching cleaved (110) face. (b) Further magnification of profile in (a).

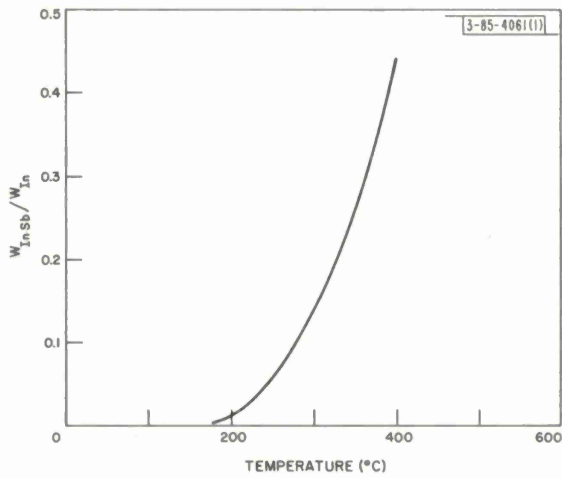


Fig. I-4. Temperature dependence of fractional weight of InSb required to produce saturated solution. (After Hall.<sup>4</sup>)

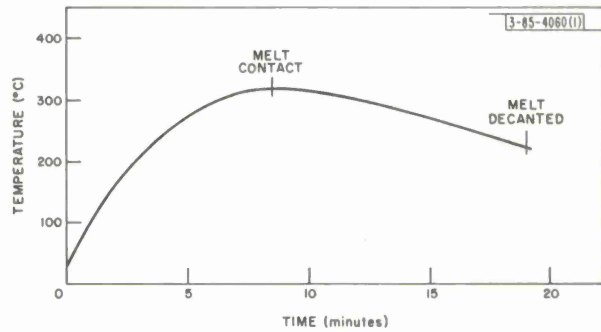


Fig. I-5. Temperature cycle of typical solution regrowth.

One application of this method was the fabrication of InSb injection lasers in which the light is emitted in a direction normal to the plane of the junction.<sup>5</sup> Such a structure is shown in Fig. I-6. The  $n^+$  layer was grown on high-resistivity p-type InSb by the above technique and the  $p^+$  layer in this case was made by zinc diffusion. In these diodes the lifetimes of injected carriers are sufficiently long ( $10^{-7}$  to  $10^{-6}$  sec) and the mobilities are sufficiently high to permit population inversion across the entire region between the contacts. The radiation which is thus generated in the active region has to pass through the doped  $p^+$  and  $n^+$  layers; hence, these have to be of good quality crystal which is transparent to the radiation. Solution regrowth proved to be the only satisfactory technique for making good  $n^+$  layers.

I. Melngailis  
A. R. Calawa

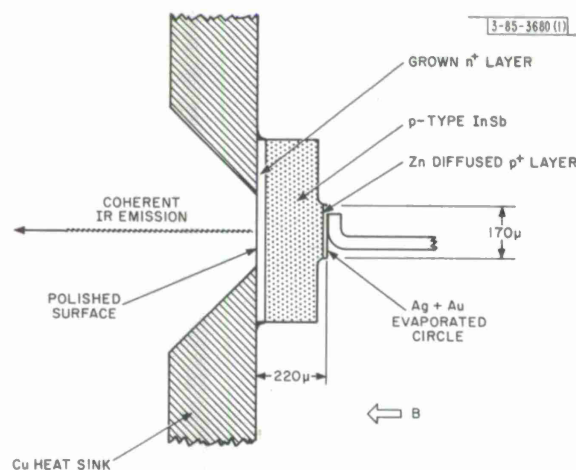


Fig. I-6. Large volume InSb injection laser designed for coherent emission normal to plane of junction.

### C. INJECTION MECHANISMS IN InSb $n^+pp^+$ STRUCTURES

We have studied experimentally the injection of carriers into InSb  $n^+pp^+$  structures similar to those used as bulk lasers.<sup>6,7</sup> In particular, we have determined the distribution of potential and electric field along the p-region at various current levels by means of a movable potential probe with the sample at 77°K. These measurements indicate that at currents less than  $1 \text{ A/cm}^2$  the dominating mechanism is the injection of electrons into the p-region from the  $n^+$  contact which causes a saturation of electron traps and an increased lifetime in the p-type bulk. At higher currents an appreciable number of holes is injected from the  $p^+$  region in order to neutralize the large number of injected electrons. This changeover from "single" to "double" injection is observed in the potential distribution as well as in the patterns of light emission at the surface of InSb lasers.

#### 1. Experimental Technique

Rectangular bars of about  $0.25 \text{ mm}^2$  cross-sectional area and lengths varying between 0.25 and 3 mm were fabricated from p-type InSb with a resistivity of about 30 to 40 ohm-cm at 77°K.

## Section I

The  $p^+$  and  $n^+$  contacts were alloyed to opposite ends of each bar; in some cases the  $n^+$  region was grown by a solution-regrowth technique. A bar was then mounted in a suitable miniature package and connected into the circuit shown in Fig. I-7. Using a movable tungsten needle probe to measure potential, current-voltage characteristics could be obtained from any number of points along the bar. The InSb bar and tungsten probe were immersed in liquid nitrogen. The probe was mounted on a micromanipulator and was viewed through a calibrated microscope. Sawtooth pulses 0.1 to 2 msec long with a repetition rate of about 100 pps were used to prevent heating.

### 2. Low Current Range

At low currents ( $0.5$  to  $1 \text{ A/cm}^2$ ) a negative resistance region is observed in the I-V characteristics shown in Fig. I-8. This negative resistance has been attributed<sup>8,9</sup> to a change in the lifetime of electrons from  $5 \times 10^{-10}$  to  $10^{-7}$  to  $10^{-6}$  sec as the deep traps (0.05 eV above the valence band)<sup>10</sup> become saturated by electrons injected from the  $n^+$  contact. The traps become saturated first near the  $n^+$  contact, and the number of conduction electrons increases sharply. As the current is increased, the electrons penetrate deeper into the p-region until the entire p-region is in the long-lifetime high-conductivity state. The potential probe measurements of Figs. I-8 and I-9 illustrate this "propagation" of the negative resistance along the bar as the current is increased. We observe an  $n^+p$  junction potential of 110 to 120 mV (Fig. I-9), whereas the  $p^+p$  contact appears ohmic in this current range. This is consistent with the electron injection model.

Figures I-10(a-b) show the potential and electric field distribution, respectively, in the p-region as obtained from the data of Fig. I-8. The field after breakdown (after the saturation of traps) is small (about 3 to 4 V/cm) and nearly constant with distance and current. The field before breakdown is nearly constant with distance but increases with current over a range of about 5 to 70 V/cm. The data of Fig. I-10(b) show that just before breakdown the measured field is slightly higher than that expected from a constant resistivity. A possible explanation of this is a variation with distance of the quasi-Fermi level for electrons due to the large variation in electron density near the boundary of the plasma. The difference in quasi-Fermi level between two points with electron densities  $n_1$  and  $n_2$  is

$$\Delta V = \frac{kT}{q} \log_e \frac{n_1}{n_2} .$$

Assuming that the probe measured this change in the Fermi level for electrons, the data of Fig. I-10 yield a  $\Delta V$  (the voltage in excess of the expected ohmic voltage drop) of about 80 to 90 mV over a distance of 0.15 mm. This value can be accounted for by a ratio  $n_1/n_2$  of  $10^5$  to  $10^6$ .

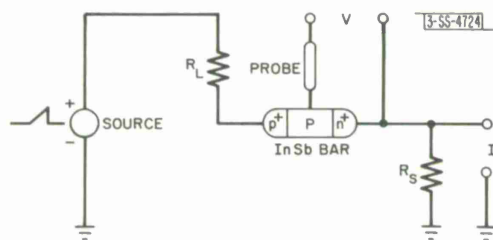


Fig. I-7. Circuit used to measure potential as a function of current at various points along InSb bar. Terminals V provide the horizontal and terminals I the vertical input to oscilloscope. Source consists of sawtooth generator and amplifier.  $R_L$  and  $R_S$  are load and current sampling resistors, respectively.

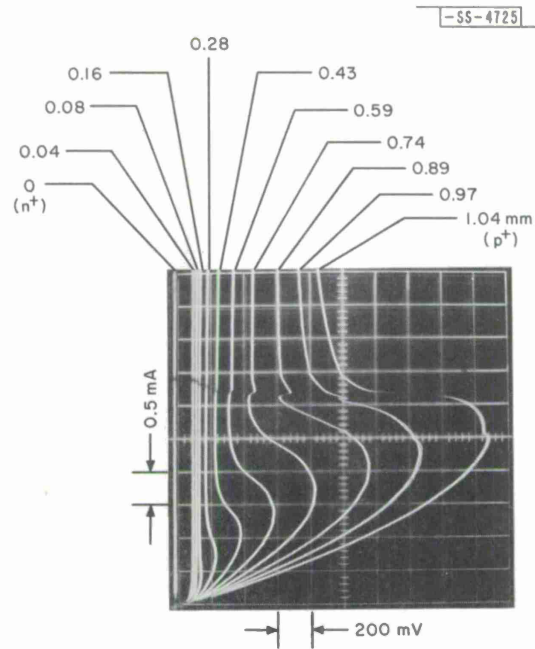


Fig. I-8. Potential as a function of current for points along InSb  $n^+p^+p^+$  device 146 at 77°K. Probe settings are given in millimeters measured across bar from  $n^+p$  junction to  $p^+p$  junction. The two traces marked  $n^+$  and  $p^+$  were obtained with probe just inside  $n^+$  and  $p^+$  regions, respectively.

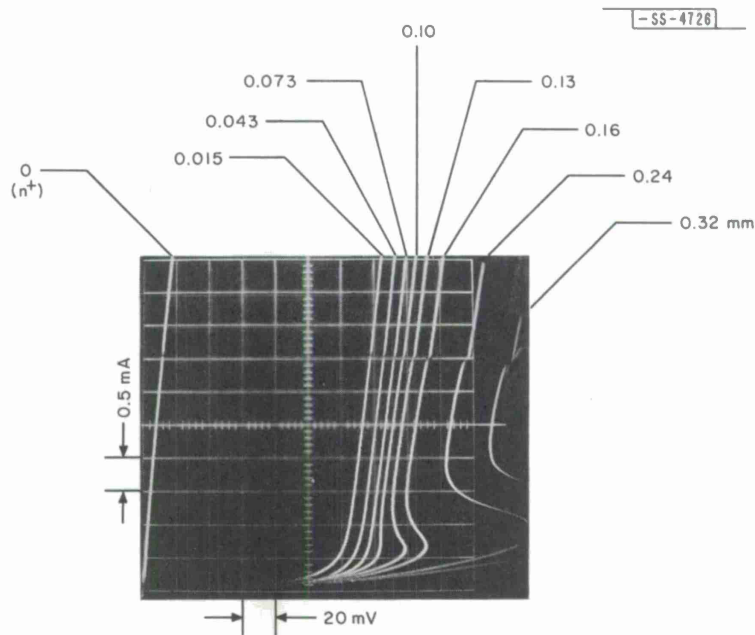


Fig. I-9. Potential as a function of current for points near  $n^+$  junction of InSb  $n^+p^+p^+$  device 146 at 77°K. Probe settings are given in millimeters measured across bar from  $n^+p$  junction. Trace marked  $n^+$  was obtained with probe just inside  $n^+$  region. Slope of this  $n^+$  trace is due to resistance between  $n^+$  contact and mount, and it is to be subtracted from slopes of remaining traces.

Section I

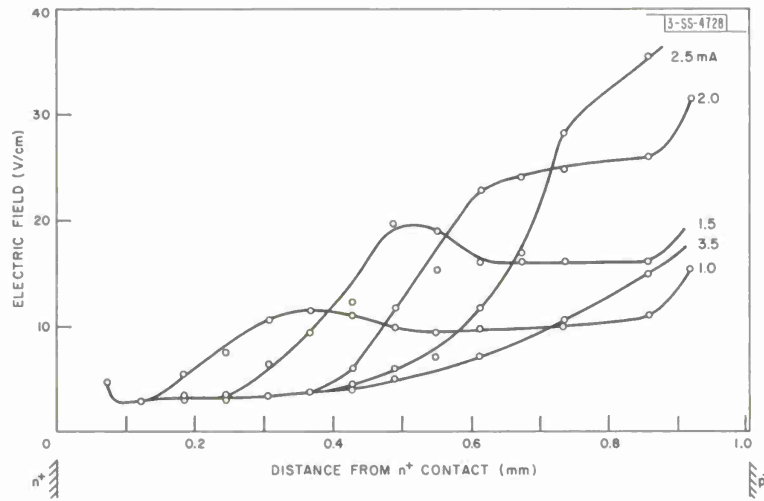
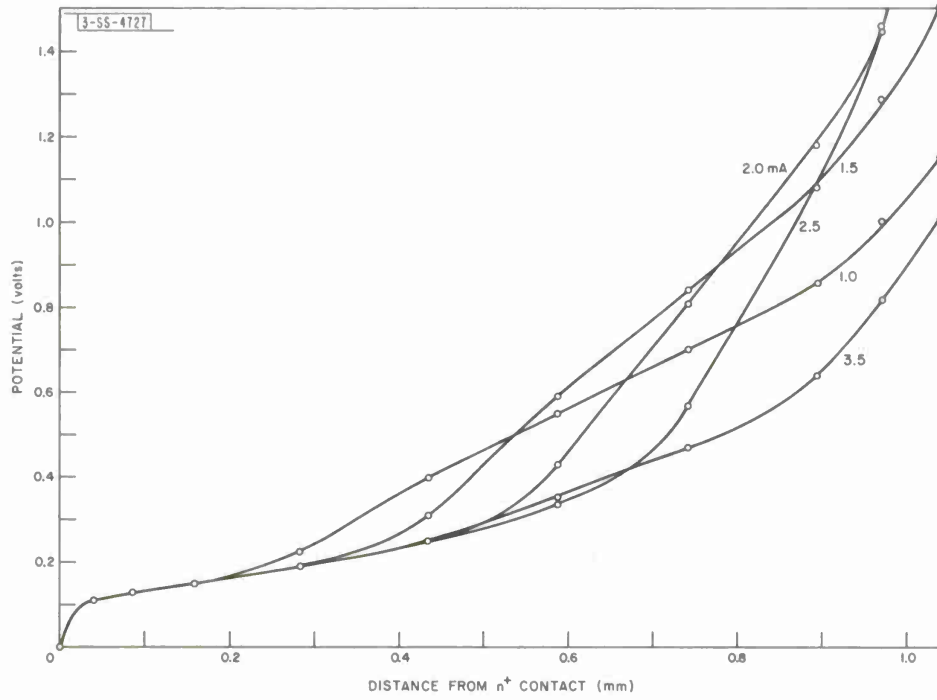


Fig. I-10. (a) Potential and (b) electric field distribution for device 146 at 77°K showing evidence of propagation of injected plasma across bar with increased current. Bar length is approximately 1 mm.

This large a ratio may be possible in regions where the lifetime changes rapidly with distance. There is also an added potential rise in regions near the  $p^+$  contact [as seen in Fig. I-10(a)] which cannot be explained by the above reasoning.

### 3. High Current Range

At currents greater than  $10 \text{ A/cm}^2$  a potential begins to develop across the  $p^+p$  junction. This potential increases in magnitude, and at current densities of  $100$  to  $200 \text{ A/cm}^2$  it becomes greater than the potential across the  $n^+p$  junction. At the same time, a low field region (which increases in length as the current increases) is seen near the  $p^+$  contact. This indicates a high carrier density near the  $p^+$  contact resulting from the injection of holes from the  $p^+$  region. Figures I-11(a-b) show the potential and field distribution, respectively, for an  $n^+pp^+$  InSb device at several current values in this range. The low field regions on both sides of the bar are evidence of the injection of carriers from both contacts, i.e., double injection. Throughout the remainder of the bar, the field is nearly constant. The combined length of the two low field regions in the 0.5-mm device is about 0.18 to 0.23 mm. This provides an estimate for the optimum length of an InSb bulk laser, since the largest possible active volume is desired, while avoiding excessive lattice and carrier heating which can occur in the high field regions of the bar in Fig. I-11.

Devices were also fabricated with a length of 0.20 to 0.25 mm. The terminal current-voltage characteristic for one of these devices is shown in Fig. I-12. The potential in the range between 1 and 500 mA appears mainly across the two junctions and the current increases exponentially with applied voltage. The field in the bulk is small ( $\leq 3 \text{ V/cm}$ ) and remains nearly constant with current. This implies that the injected carrier density increases linearly with current in this range. However, above 1 A ( $\approx 300 \text{ A/cm}^2$ ) the field in the bulk begins to increase ( $15$  to  $25 \text{ V/cm}$  at 9 A).

The preceding low and high current data are consistent with the spontaneous emission patterns observed at the surface of InSb bulk lasers at  $11^\circ\text{K}$ . In Fig. I-13, at 20 mA the brightest spot and hence the greatest injected carrier density is near the  $n^+$  contact, from which electrons are injected. At 50 mA a second bright spot appears near the  $p^+$  contact, consistent with hole injection. As the current is further increased to 250 mA, the light intensity and hence the carrier density near the  $p^+$  contact increases faster than the density near the  $n^+$  contact.

R. W. Knepper  
I. Melngailis

### D. BULK GaAs MICROWAVE AMPLIFIERS

Microwave amplification similar to that recently reported by Thim, *et al.*,<sup>11</sup> but exhibiting some significant differences in frequency and threshold conditions, has been observed in samples of n-GaAs at room temperature.

All the samples were 50- $\mu$ -long pieces of n-GaAs with a mobility of about  $5000 \text{ cm}^2/\text{V-sec}$  and a resistivity of approximately  $100 \text{ ohm-cm}$ . Ohmic contacts were made to opposite sides of the sample by alloying tin at  $400^\circ\text{C}$  in a hydrogen and HCl atmosphere. The samples were mounted in a varactor diode package and placed at the end of a 50-ohm coaxial line. The reflection gain was then measured as a function of frequency and (pulsed) bias voltage. The gain

Section I

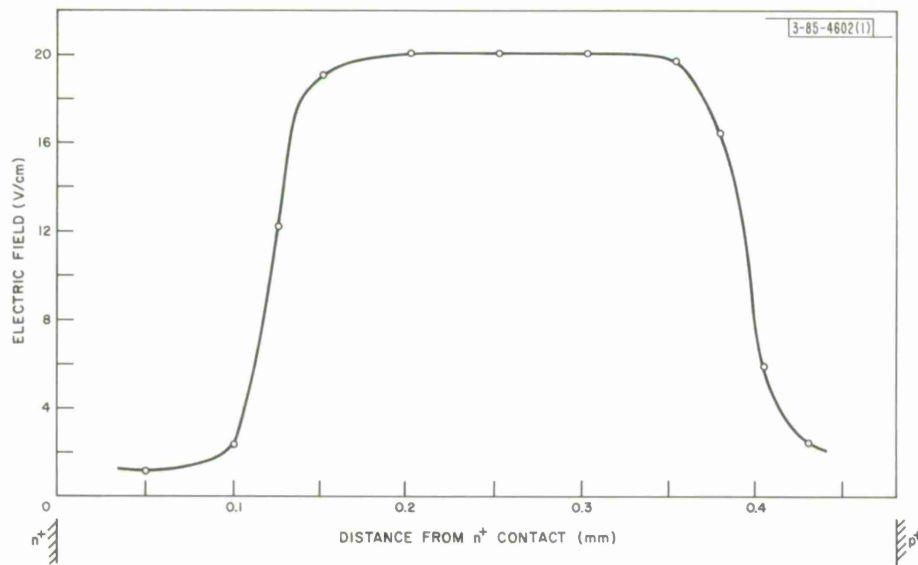
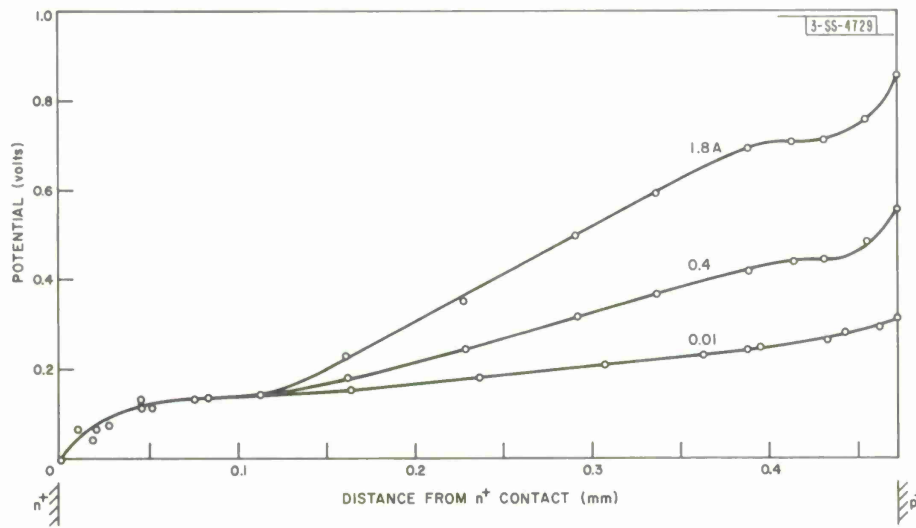
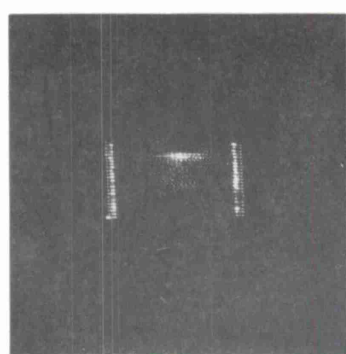
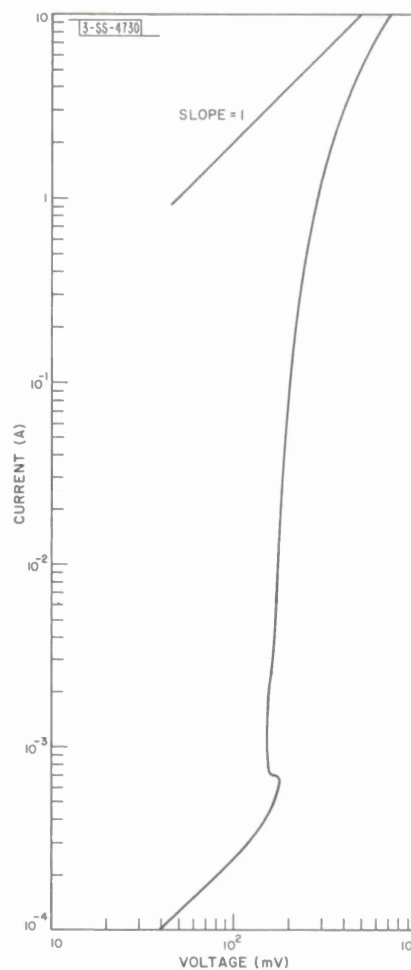
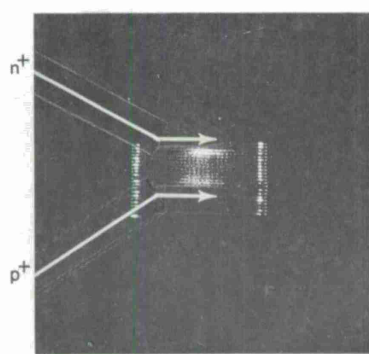


Fig. I-11. (a) Potential and (b) electric field distribution for device 153 at 77°K showing carrier injection from both junctions. Bar length is approximately 0.5 mm.

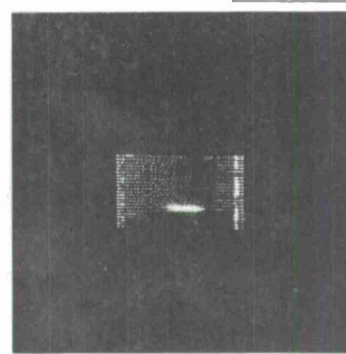
Fig. I-12. Variation of current with total voltage (including junction potentials) for device 162 at 77°K. Bar length is 0.22 mm.



20 mA



50 mA



250 mA

Fig. I-13. Spontaneous radiation patterns of an  $n^+pp^+$  InSb structure with 400- $\mu$ -long bar-shaped p-region obtained at 11°K with three different values of current. Diode cross section was  $10^{-3}$  cm<sup>2</sup>. Sensitivity of image converter was reduced as current was increased.

Section I

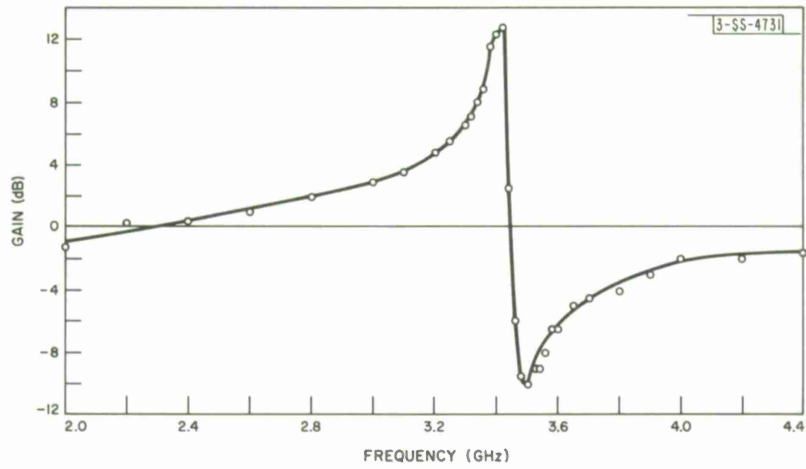


Fig. I-14. Reflection gain as a function of frequency for an applied voltage of 35 volts across 50- $\mu$ -long sample of n-GaAs, whose room-temperature resistivity was 100 ohm-cm.

-85-4614-1

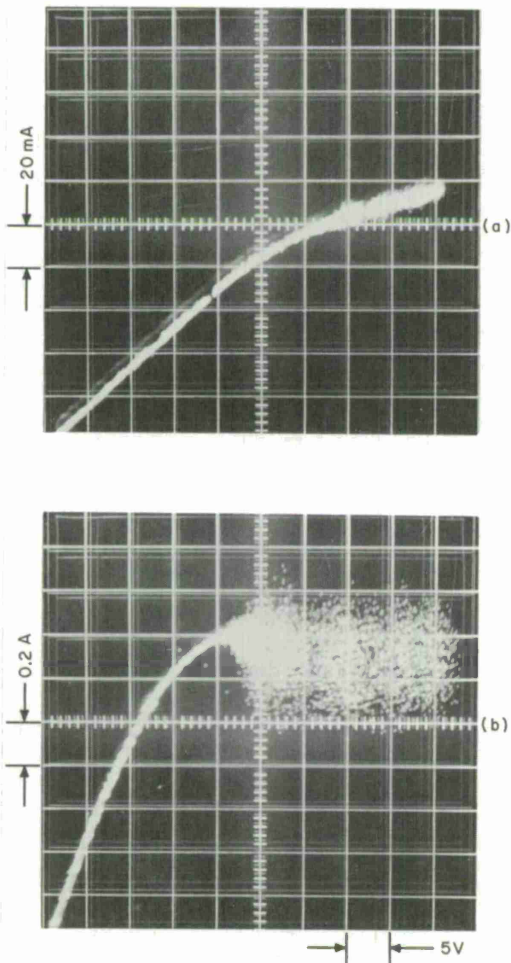


Fig. I-15. Current-voltage characteristics for 50- $\mu$ -long samples of n-GaAs: (a) sample whose room-temperature resistivity was 100 ohm-cm, and which exhibited gain vs frequency curve shown in Fig. I-14; and (b) sample whose room-temperature resistivity was 1 ohm-cm, and which did not exhibit amplification.

remained negative (loss) from zero applied voltage to about 30 volts. Above 30 volts, gain was observed at frequencies near 3 GHz, as shown in Fig. I-14 for a sample biased at 35 volts. For biases greater than 36 volts the amplifier output became noisy, and above 40 volts the sample oscillated spontaneously with a center frequency coincident with the peak of the gain curve. The saturation output power of this sample was about  $-10$  dBm, consistent with the dynamic range reported by Thim, *et al.*,<sup>11</sup> and the noise figure at the peak of the gain curve was about 17 dB for 10 dB of gain. No gain was observed at the second harmonic of the gain peak.

The frequency at which the gain peak occurs agrees fairly well with the frequency at which Gunn oscillations<sup>12</sup> occur in lower resistivity samples of the same length, in contrast to the results of Thim, *et al.*, who found the frequency of the gain peak to be about twice the Gunn frequency. Also, the average applied electric field necessary for gain is about 7000 V/cm – twice the value reported by Thim, *et al.* Both these differences can be explained if the electrical length of the samples used by Thim, *et al.*, is much shorter than the physical length.

In Fig. I-15, the current-voltage curve for the sample of Fig. I-14 is shown and compared with that for a sample of the same length ( $50\mu$ ) but lower resistivity (1 ohm-cm) which exhibited oscillation but not amplification. We see that the amplifier sample exhibits only a slight tendency toward current saturation with increasing voltage, whereas the oscillator sample begins to saturate even below the threshold of oscillation, and above threshold exhibits a range of current oscillation relatively independent of voltage.

The existence of a positive resistance in the amplifier samples for average applied electric fields much higher than the field at which Gunn oscillation normally occurs suggests that the usual domain formation does not take place in these high-resistivity samples. This agrees with recent calculations of McCumber and Chynoweth<sup>13</sup> who have found that, for sufficiently small products of carrier concentration and sample length, the transferred electron effect leads to a negative conductance at frequencies near the reciprocal of the transit time even though the DC solution displays only positive resistance.<sup>14</sup>

A. G. Foyt  
T. M. Quist

REFERENCES

1. H. Nelson, RCA Review 24, 603 (1963).
2. A. J. Strauss, J. Appl. Phys. 30, 559 (1959).
3. J. T. Edmond, Proc. Phys. Soc. (London) 73, 622 (1959).
4. R. N. Hall, J. Electrochem. Soc. 110, 385 (1963).
5. I. Melngailis, Appl. Phys. Letters 6, 59 (1965), DDC 613903.
6. I. Melngailis, R. J. Phelan, and R. H. Rediker, Appl. Phys. Letters 5, 99 (1964).
7. I. Melngailis, Appl. Phys. Letters 6, 59 (1965).
8. I. Melngailis and R. H. Rediker, J. Appl. Phys. 33, 1892 (1962).
9. \_\_\_\_\_, Proc. IRE 50, 2428 (1962).
10. R. A. Laff and H. Y. Fan, Phys. Rev. 121, 53 (1961).
11. H. W. Thim, M. R. Barber, B. W. Hakki, S. Knight, and M. Uenohara, Appl. Phys. Letters 7, 167 (1965).
12. J. B. Gunn, IBM J. Research Develop. 8, 141 (1964).
13. D. E. McCumber and A. G. Chynoweth, IEEE Trans. Electron Devices (to be published, January 1966).
14. W. Shockley, Bell System Tech. J. 33, 799 (1954).

## II. LASER RESEARCH

### A. NONCONVECTIVE INSTABILITIES IN RAMAN MEDIA

An investigation of the dispersion relation for infinite homogeneous Raman media reveals that such media do not support nonconvective instabilities near the Stokes or anti-Stokes frequencies, but there do appear to be such unstable modes in the vicinity of  $\omega = 0$ ,  $\vec{k} = 0$  and  $\omega = 2\omega_L$ ,  $\vec{k} = 2\vec{k}_L$ , where  $\omega_L$  and  $\vec{k}_L$  are the laser frequency and wave vector, respectively. The time constant for the growth of these instabilities is on the order of milliseconds. Because the assumed dispersion relation describing the medium is not reliable for these values of  $\omega$  and  $\vec{k}$ , it is likely that these instabilities have no physical significance.

R. S. Sorbello  
H. A. Haus\*

### B. SELF-FOCUSING OF OPTICAL BEAMS

The possibility has been noted of the self-trapping of optical frequency electromagnetic beams due to a nonlinear index of refraction, and various physical mechanisms which could give rise to the nonlinearity have been discussed.<sup>1-3</sup> Trapped modes have been found.<sup>3-5</sup> Beam trapping is expected to have important effects on other phenomena occurring in intense beams.

Here we examine the possibility of an increase in intensity of the central region of the beam as a function of distance in the direction of propagation (self-focusing). We take Eq. (3) of Ref. 3 as our starting equation,

$$\nabla^2 \vec{E} - \frac{\epsilon_0}{c^2} \frac{\partial^2 \vec{E}}{\partial t^2} - \frac{\epsilon_2}{c^2} \frac{\partial^2 (\vec{E} \cdot \vec{E})}{\partial t^2} = 0 \quad , \quad (1)$$

where  $\epsilon_0$  and  $\epsilon_2$  are real, and  $\epsilon_2 E^2 \ll 1$ . We assume a linearly polarized wave of frequency  $\omega$  and propagating along the z-axis, and obtain the approximate equation

$$2ik \frac{\partial E'}{\partial z} + (\nabla_x^2 + \nabla_y^2) E' + \frac{\epsilon_2' k^2}{\epsilon_0} |E'|^2 E' = 0 \quad , \quad (2)$$

where  $\epsilon_2' = 3\epsilon_2/4$ , and  $E'$  is the slowly varying part of  $E$  such that  $E = E' \exp(ikz - i\omega t)$ . Equation (2) employs a familiar approximation of optics and has been used by Vainshtein<sup>6</sup> in solving the resonator problem. It is valid when the distance characteristic of the change of  $E'$  in the z direction is much larger than a wavelength. The equation is a parabolic type and can be solved with an open boundary.

From Eq. (2) we obtain a focusing distance

$$z = z_{\text{focus}} \equiv \frac{1}{2} a \sqrt{n_0/n_2'} / E'_m \quad (3)$$

---

\*Department of Electrical Engineering and Research Laboratory of Electronics, M.I.T.

## Section II

where  $a$  is a characteristic transverse radius of curvature of the input beam intensity and  $E'_m$  is the peak field value. The focusing distance is defined assuming an equiphase input beam. It is not expected that the solution for the beam center will be strictly correct for distances within a few wavelengths of the focusing distance because of the neglect of the second derivative in Eq. (2).

To verify these considerations, Eq. (2) is solved numerically for a cylindrically symmetrical beam. To facilitate this, Eq. (2) is rewritten in the following dimensionless form

$$i \frac{\partial E^*}{\partial z^*} + \frac{\partial^2 E^*}{\partial r^{*2}} + \frac{1}{r^*} \frac{\partial E^*}{\partial r^*} |E^*|^2 E^* = 0 \quad (4)$$

where  $r^* = r/a$ ,  $z^* = z/2ka^2$ , and  $E^* = \sqrt{\epsilon_2/\epsilon_0} kaE'$ . The starred notation for the dimensionless quantities is similar to that of Ref. 3; it does not indicate complex conjugation. In this dimensionless form,  $z^*_{\text{focus}} = (2\sqrt{2} E'_m)^{-1}$ .

We have solved Eq. (4) by a finite difference or mesh technique discussed by Harmuth<sup>7</sup> and modified to include the nonlinearity. An equiphase Gaussian intensity profile was assumed for the input beam. An example of the numerical results obtained on an SDS 930 computer is given in Fig. II-1.  $E'_m$  was chosen large enough to give a fairly small focusing distance.

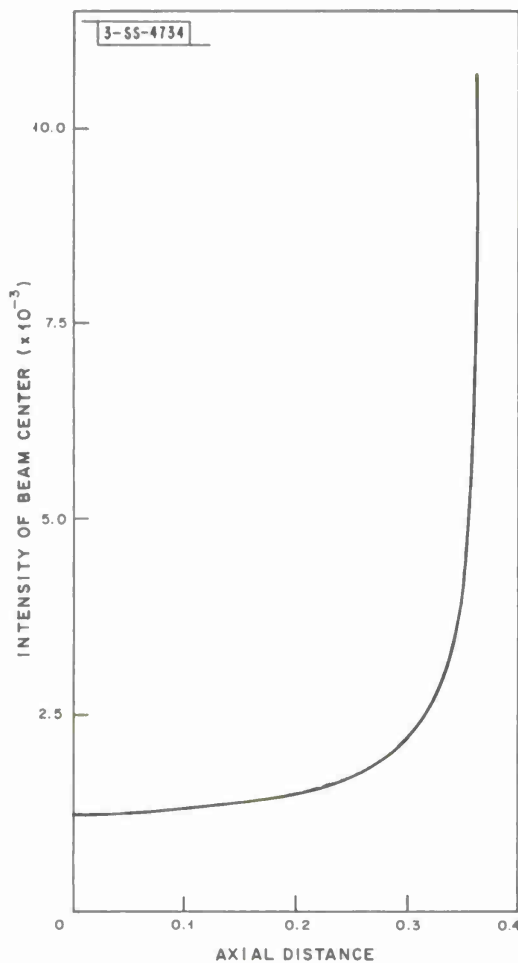


Fig. II-1. Calculated intensity of beam center  $I_m^*$  vs  $z^*$  (in units of  $1/E_m^*$ ).

The curve in Fig. II-1 is given to a high accuracy by

$$I_m^*(z^*)/I_m^*(0) = z_0^*(z_0^{*2} - z^{*2})^{-1/2} \quad (5)$$

where  $I_m = |E_m|^2$ . We find that  $z_0^* = 0.366/E_m^*(0)$ , while from Eq. (3)  $z_{\text{focus}}^* = 0.353/E_m^*(0)$ .

P. L. Kelley

### C. HIGH POWER LASER EFFECTS IN LIQUIDS

Dielectric breakdown was observed in water by focusing a ruby laser beam. There is blue emission from the focus, less prominent than in air breakdown with the same laser output and lens, but visible through a blue filter. The breakdown has a threshold at about 1-MW laser power, where the blue emission changes rapidly with slight changes of laser power. At lower powers the blue emission is no longer detected, either visually or with a photomultiplier. The blue emission has a half-duration measured as 20 nsec, instrument limited, and has a much longer weak afterglow. Spectral distribution of the emission was measured in the transverse direction from 3200 to 4500 Å, with a minimum at 3600 Å. The rise toward longer wavelengths corresponds to the region of the Balmer lines of hydrogen. The reason for the relative inconspicuousness of the blue emission may be that the Balmer series occurs mainly at longer wavelengths, extending to 6563 Å. Purification of the water shows a possible increase in threshold power, but does not affect the spectral distribution.

Fluorescence from limonene ( $C_{10}H_{16}$ ) was induced by a laser beam, presumably by multiple-photon absorption, and observed in the forward direction. In the wavelength range studied, 3200 to 4500 Å, fluorescence occurs as a band from 4000 to 4500 Å and beyond, and agrees with the normal fluorescence observed on a spectrofluorometer. The horizontal polarization  $P_h$  is about twice the vertical polarization  $P_v$ , when observed with incident horizontally polarized light. An approximate classical theory,<sup>8</sup> describing a molecule in the liquid as two different anisotropic oscillators, one polarized by the incident light and the other radiating while polarized at some other orientation, and including the Brownian rotation of the excited molecule during the lifetime, gives the polarization

$$p = \frac{P_h - P_v}{P_h + P_v} \quad \text{as} \quad p = p_0 \left[ 1 + \left( 1 - \frac{1}{3} p_0 \right) \frac{kT}{\eta V} \tau \right]^{-1}; \quad (6)$$

$V$  is the molecular volume,  $\eta$  the viscosity,  $\tau$  the lifetime of the fluorescent state, and  $-1/3 \leq p_0 \leq 1/2$ . With  $p = 1/3$  and  $\eta = 0.02$  poises, one concludes from the smallness of the depolarization due to Brownian motion that  $\tau < 10^{-9}$  sec. This is consistent with the measurement, for which  $\tau < 2 \times 10^{-8}$  sec, instrument limited.

A theoretical examination has been made of emission of sum frequency light which is incoherent with the primary light, in order to deduce the mechanisms of this emission. It was shown that density fluctuation scattering is not allowed by the symmetry of the molecular polarizability tensors, except for optically active molecules, and even then only when the two primary frequencies are different. In other cases, therefore, the unshifted sum frequency emission must arise from orientation fluctuations.

D. L. Weinberg

## D. HIGH POWER BRILLOUIN AND RAMAN SCATTERING IN SOLIDS

After completing the stimulated Brillouin scattering experiment in quartz,<sup>9</sup> it was decided to look for stimulated Raman scattering in quartz in order to study possible interference between the Raman and Brillouin effects at high incident ruby laser powers. Heretofore, the threshold for stimulated Raman scattering had been reached in only a very few solids (calcite, sulfur, diamond), and quartz appeared to have a particularly high threshold.

Figure II-2 shows the spectrum of quartz photographed in the forward direction ( $E \parallel c$ -axis) with a Bausch and Lomb spectrograph under approximately 200-MW ruby laser excitation focused with a 13-cm lens along the x-axis. On the original film, four stimulated Stokes and two anti-Stokes lines are observable with the following wave-number shifts.

$$\begin{aligned} S_1 &= 459 \text{ cm}^{-1} & AS_1 &= 465 \text{ cm}^{-1} \\ S_2 &= 921 \text{ cm}^{-1} & AS_2 &= 930 \text{ cm}^{-1} \\ S_3 &= 1382 \text{ cm}^{-1} \\ S_4 &= 1846 \text{ cm}^{-1} \end{aligned}$$

All measurements are to  $\pm 1 \text{ cm}^{-1}$ . The above shifts are due to totally symmetric class-A vibrations, which are completely polarized.

The difference of the first Stokes shift from  $466 \text{ cm}^{-1}$ , the most intense line in the quartz spectrum measured by classical Raman spectroscopy methods,<sup>10</sup> seems to be real. The spontaneous line<sup>11</sup> is at least  $6 \text{ cm}^{-1}$  wide, and sometimes the weaker  $452 \text{ cm}^{-1}$  line appears on the wings of the  $466 \text{ cm}^{-1}$  line. Furthermore, frequency shifts of a few wave numbers of some of the quartz Raman lines have been noted with changes in relative orientation of the optic axis with respect to plane of scattering.<sup>12</sup> Finally, first overtones observed in the spontaneous spectrum<sup>10</sup> fall into a broad band consisting of harmonic and combination lines of  $466 \text{ cm}^{-1}$  and its satellites, while second overtones are not observed at  $1398 \text{ cm}^{-1}$  ( $3 \times 466 \text{ cm}^{-1}$ ) but rather at  $1381 \text{ cm}^{-1}$ , as in the present experiment. No spontaneous lines have ever been reported in the vicinity of  $1864 \text{ cm}^{-1}$  ( $4 \times 466 \text{ cm}^{-1}$ ), whereas spontaneous  $AS_2$  cannot be observed because of absence of thermal excitation.

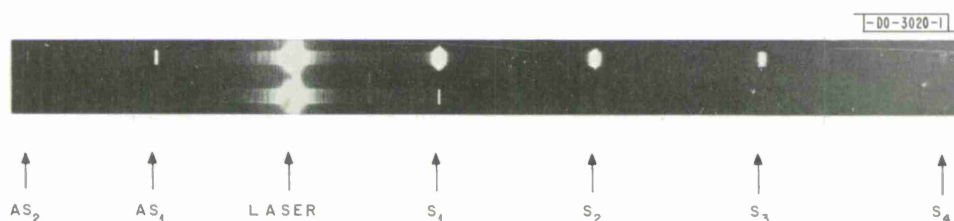


Fig. II-2. Stimulated Raman spectrum of quartz photographed with 1.5-m Bausch and Lomb spectrograph. Ruby laser power was approximately 200 MW.

An interesting property of quartz is that the dispersion is very small in the spectral region around the ruby laser wavelength. In fact, even though  $dn/d\lambda$  curves slightly,  $dn/dk$  is virtually flat. This means that phase matching is determined by the usually small secondary term in the

phase-matching condition, and  $AS_1$  is observed practically in the forward direction. Since the selection rules do not a priori forbid scattering from one kind of polarization to another, it might be possible to observe phase-matched extraordinary  $AS_1$  radiation excited from incident laser radiation polarized as an ordinary ray. This process would occur at a relatively large scattering angle.

P. E. Tannenwald  
F. H. Perry

#### E. PHOTOELECTRON STATISTICS PRODUCED BY LASER OPERATING BELOW THRESHOLD OF OSCILLATION

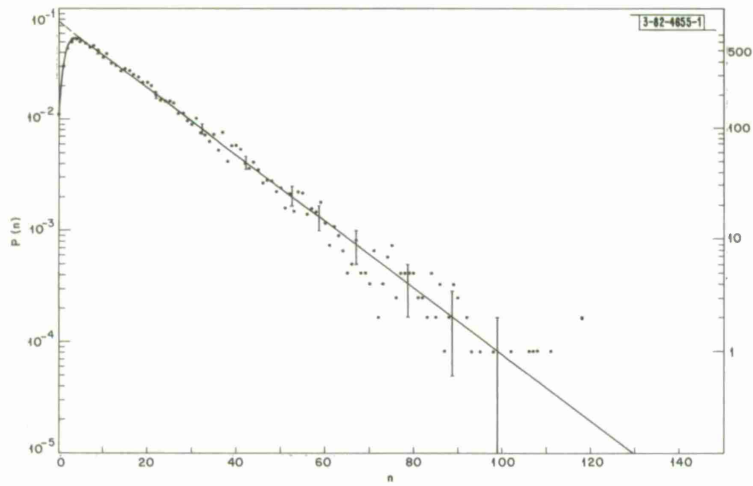
When narrow-band Gaussian light is incident upon a photomultiplier, the probability distribution of the photoelectrons emitted within a time interval short compared to the inverse bandwidth of the light should follow the Bose-Einstein distribution.<sup>13-17</sup> Until the advent of the laser, it was not possible to make counting measurements within time intervals short compared to the inverse bandwidth of the light. A laser operating slightly below threshold may emit narrow-band light with a Gaussian amplitude distribution centered about one frequency, provided one axial mode is sufficiently near the threshold of oscillation so that its gain is high enough compared to the other modes to make it dominant. By "Gaussian amplitude distribution" of the light amplitude, we mean that the light is describable in Glauber's  $P(\alpha)$  representation<sup>15,16</sup> in which each mode has a  $P(\alpha)$  function of the form

$$P(\alpha) = (1/\pi\bar{n}) \exp(-|\alpha|^2/\bar{n}) \quad (7)$$

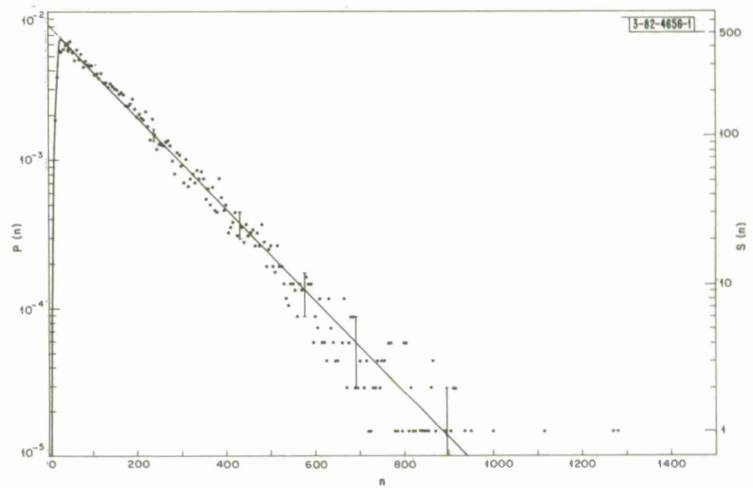
For the experiments to be reported we used a helium-neon gas laser operating at  $6328 \text{ \AA}$  with internal mirrors of hemispherical geometry and reflectivities of greater than 99 percent.

By monitoring the spectrum of the photomultiplier current produced by the light, we adjusted the laser to operate slightly below threshold with a light bandwidth of approximately 380 Hz. In an experimental environment the vibrations of the mirror mounts introduce frequency fluctuations which cause deviations of the light from an ideal narrow-band Gaussian waveform. Frequency fluctuations are not detected in a photomultiplier homodyne detector and, with proper care, the influence of frequency fluctuations may be negligible, as demonstrated experimentally in Ref. 18. It is legitimate, therefore, to treat the waveform emitted from the laser as an essentially ideal narrow-band Gaussian waveform. The power output of the laser was stabilized<sup>19</sup> against long-term drifts by a feedback network with a time constant of the order of  $2 \times 10^{-2}$  sec. In order to reduce background, the light was passed through a polarizer adjusted for maximum transmission. Photoelectrons emitted in the photomultiplier were counted in a high-speed counter with a double pulse resolution time of about  $14 \times 10^{-9}$  sec. Three sets of data were taken for counting intervals of  $10^{-5}$ ,  $10^{-4}$ , and  $10^{-3}$  sec, respectively. The number of photoelectrons observed in successive time intervals was recorded on tape and then processed by a computer. Approximately 13,000 samples were taken for each of the three counting intervals shown in Fig. II-3. If the laser output indeed consisted of a pure narrow-band Gaussian light centered at a single frequency, the probability of observing exactly  $n$  photoelectrons within a time interval short compared to the inverse bandwidth would follow the familiar Bose-Einstein Distribution Law.

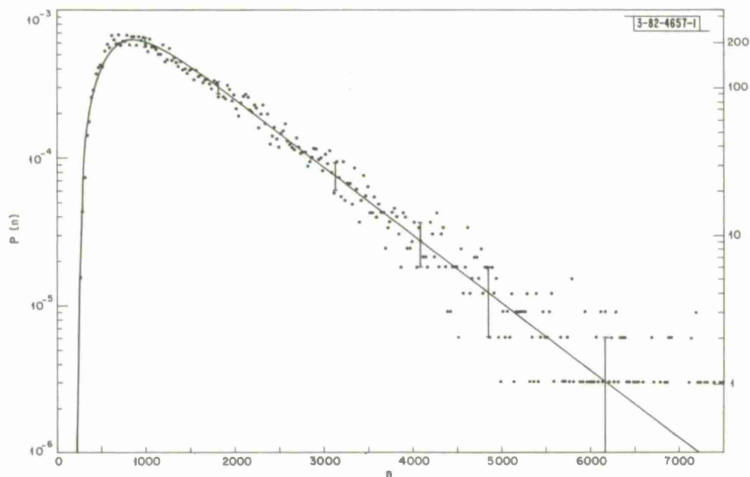
Section II



(a) Counting interval  $T = 10^{-5}$  sec;  
12,251 samples.



(b) Counting interval  $T = 10^{-4}$  sec;  
13,619 samples.



(c) Counting interval  $T = 10^{-3}$  sec;  
13,093 samples.

Fig. II-3. Probability distribution and number of observed samples vs photoelectron count.

$$P(n) = (1 + \bar{n})^{-1} (1 + 1/\bar{n})^{-n} \quad (8)$$

where  $\bar{n}$  is the average count. On the semilog plot of Fig. II-3(a), this should appear as a straight line. The figure shows that the experimental points lie on or about a straight line down to counts of the order of 4. At lower counts the experimentally observed points deviate from the theoretical curve, owing to admixture of other modes at other frequencies. If we assume that these other modes are broad-band, and therefore effectively produce a Poisson probability distribution of their own, a probability distribution slightly different from the Bose-Einstein distribution is calculated to be

$$P(n) = (1 + \bar{n}_m)^{-1} (1 + 1/\bar{n}_m)^{-n} \exp(\bar{n}_b/\bar{n}_m) \frac{\int_{n'_b}^{\infty} e^{-u} u^n du}{n!} \quad (9)$$

where  $\bar{n}_m$  and  $\bar{n}_b$  are the average photoelectron counts due to the narrow-band mode and the broad-band background, respectively, and  $\bar{n}_b = \bar{n}_m (1 + 1/\bar{n}_m)$ . Because the dominant mode is linearly polarized, the background can be estimated from the degree of polarization of the outgoing light. Since the background is generally unpolarized, it has twice the intensity of the light polarized perpendicular to the polarization of the dominant mode. In this way an experimental estimate of the background can be made. By measuring the ratio of polarized to unpolarized light, we found that the average total photoelectron count within  $10^{-5}$  sec was 15.8, of which the dominant mode and the background counts were 14 and 1.8, respectively. Introducing these values into Eq. (9) results in the theoretical curve shown as a solid line in Fig. II-3(a). Agreement between this theoretical curve and the experimental results is evident. The experimental points are scattered because a finite number of samples was taken. The scattering should show a mean-square deviation proportional to the square root of the number of samples taken. The predicted spread is indicated by vertical bars in the figures. The vertical scale given for  $S(n)$  on the right side of Fig. II-3 indicates the number of samples observed for any given photoelectron count  $n$ . For high values of  $n$ , near the "tail" end of the figure, the number of samples observed is naturally small and therefore the predicted spread indicated by the vertical bars becomes large. Also, the arrangement of all experimental points along horizontal lines which correspond to the integer values of  $S(n)$  becomes very noticeable. In order to simplify the plotting of data and to reduce the scatter, the experimental points shown in Figs. II-3(b) and (c) are based on the averages of 5 and 25 adjacent data points, respectively. Figure II-3(b) shows the results obtained for a counting interval of  $10^{-4}$  sec. The average values of photoelectron counts used in Eq. (9) to compute the theoretical curve indicated by a solid line in Fig. II-3(b) were 159, 140, 19 for the total, the dominant mode, and the background, respectively, within the  $10^{-4}$ -sec counting interval. Figure II-3(c) shows the corresponding observations for a counting interval  $T = 10^{-3}$  sec, which is longer than the inverse bandwidth (in radians) of the light (approximately  $4.2 \times 10^{-4}$  sec for Fig. II-3). In this range an asymptotic expression developed by R. J. Glauber<sup>20</sup> is applicable,

$$P(n) = (\bar{n}/\sqrt{2\pi\mu}) (n)^{-3/2} \exp[-(\sqrt{n} - \bar{n}/\sqrt{n})^2/2\mu] \quad (10)$$

## Section II

where  $\mu = w/\gamma$ ,  $\gamma$  is the linewidth,  $w$  is the average rate of photoelectron counts, and  $\bar{n}$  is the average photoelectron count within the counting time interval  $T$ . The inverse light bandwidth is determined from the spectral measurement and all other parameters in this equation are obtained from the photoelectron counting experiment. Inserting these values into Eq. (10), we obtain the theoretical curve shown as a solid line in Fig. II-3(c). The shape of the probability distribution is not sensitive to small admixtures of broad-band modes when the time interval becomes comparable to the inverse bandwidth. Therefore, the equation developed by Glauber need not be corrected for the background modes. Glauber's equation holds for counting intervals long compared to the inverse bandwidth. In the present example, the counting interval is 2.4 times longer than the inverse bandwidth, yet the fit of Glauber's formula is satisfactory.

The authors believe that Fig. II-3(a) shows the first experimental measurement of a Bose-Einstein probability distribution of photoelectrons. Also, the results shown in Fig. II-3(c) constitute the first experimental test of Eq. (10).

A determination of the probability distribution of photoelectron counts has been reported by Johnson, McLean, and Pike,<sup>21</sup> using an incoherent light source and, therefore, counting intervals much longer than the inverse bandwidth. Their work provided the initial impetus for the measurements reported here.

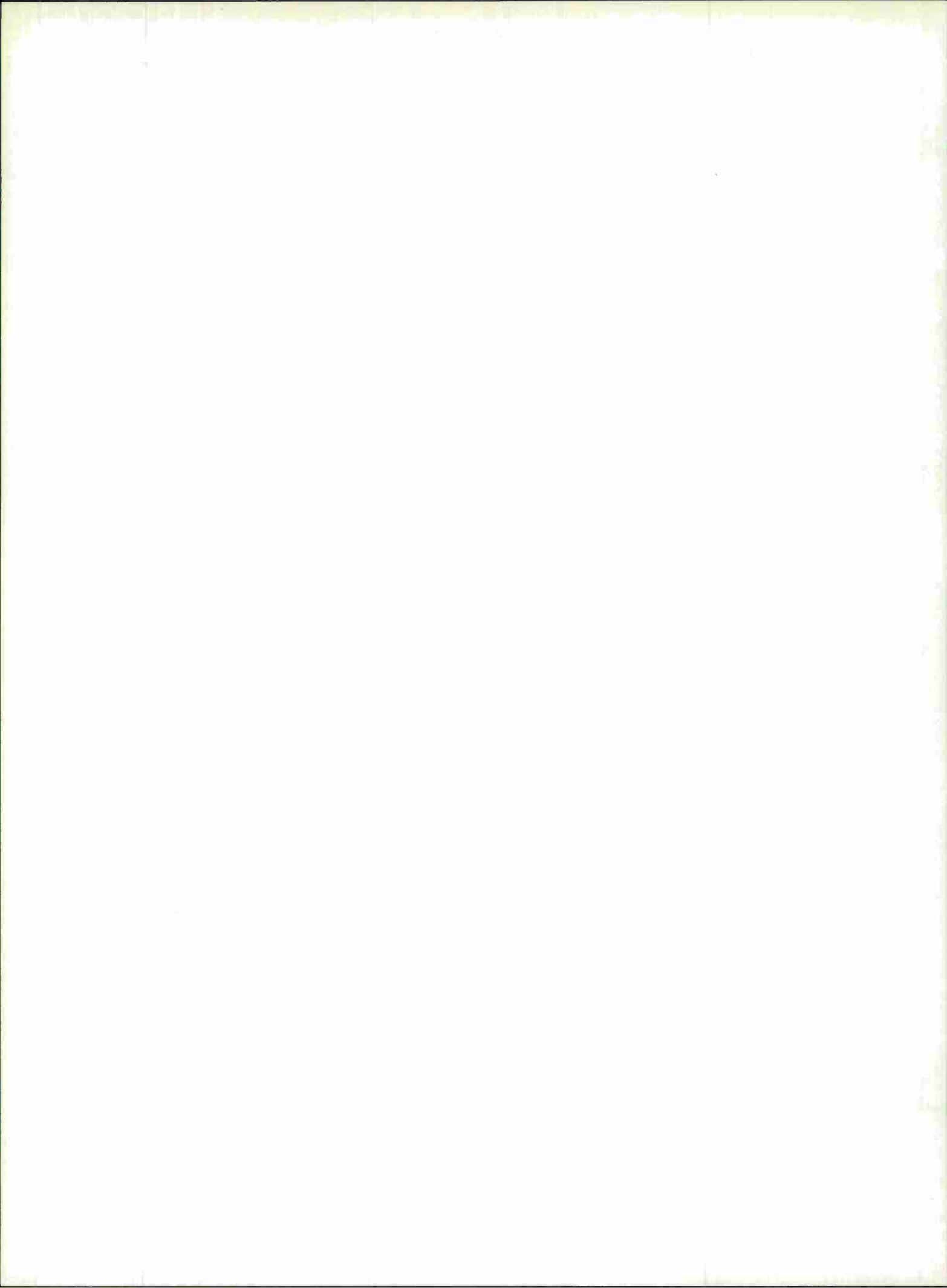
C. Freed  
H. A. Haus\*

---

\* Department of Electrical Engineering and Research Laboratory of Electronics, M.I.T.

## REFERENCES

1. G. A. Askar'yan, Zhur. Eksp. i Teoret. Fiz. 42, 1567 (1962) [translation: Soviet Phys. - JETP 15, 1088 (1962)].
2. V. I. Talanov, Izv. Vysshikh Uchebn. Zavedenii, Radiofiz. 7, 564 (1964) [translation: Radiophysics 7, 254 (1964)].
3. R. Y. Chiao, E. Garmire, and C. H. Townes, Phys. Rev. Letters 13, 479 (1964).
4. Z. Jankauskas, to be published.
5. H. A. Haus, private communication.
6. L. A. Vainshtein, Zh. Tekhn. Fiz. 34, 193 (1964) [translation: Soviet Phys. - Tech. Phys. 9, 157 (1964)].
7. H. F. Harmuth, J. Math. and Phys. 36, 269 (1957).
8. P. Pringsheim, Fluorescence and Phosphorescence (Interscience, New York, 1949), p. 370.
9. Solid State Research Report, Lincoln Laboratory, M. I. T. (1965:2), pp. 23-26, DDC 624611.
10. D. Krishnamurti, Proc. Indian Acad. Sci. 47A, 276 (1958).
11. V. G. Zubov and L. P. Osipova, Kristallografiya 6, 418 (1961) [translation: Soviet Phys. - Cryst. 6, 330 (1961)].
12. J. P. Mathieu, Compt. rend. 234, 1961 (1952).
13. L. Mandel, Proc. Phys. Soc. (London) 72, 1037 (1959).
14. E. Wolf, Proc. Symposium on Optical Masers, Polytechnic Institute of Brooklyn 13, (Polytechnic Press, 1963), p. 29.
15. R. J. Glauber, Phys. Rev. 130, 2529 (1963).
16. \_\_\_\_\_, Phys. Rev. 131, 2766 (1963).
17. P. L. Kelley and W. H. Kleiner, Phys. Rev. 136, A316 (1964).
18. C. Freed and H. A. Haus, Appl. Phys. Letters 6, 85 (1965).
19. \_\_\_\_\_, Phys. Rev. 141, 287 (1966).
20. R. J. Glauber, Physics of Quantum Electronics, P. L. Kelley, B. Lax, P. E. Tannenwald, Eds. (McGraw-Hill, New York, to be published).
21. F. A. Johnson, T. P. McLean, and E. R. Pike, Physics of Quantum Electronics, P. L. Kelley, B. Lax, P. E. Tannenwald, Eds. (McGraw-Hill, New York, to be published).



### III. MATERIALS RESEARCH

#### A. Hg-Te PHASE DIAGRAM

Differential thermal analysis has been used to measure liquidus temperatures for the portions of the Hg-Te system from 3 to 25 and from 50 to 100 atomic-percent tellurium. Liquidus points between 30 and 60 atomic-percent tellurium were obtained previously<sup>1</sup> from data on the partial pressures of Hg(g) and Te<sub>2</sub>(g) in equilibrium with Hg-Te condensed phases. The two sets of liquidus points have been combined to establish the phase diagram for the Hg-Te system shown in Fig. III-1.

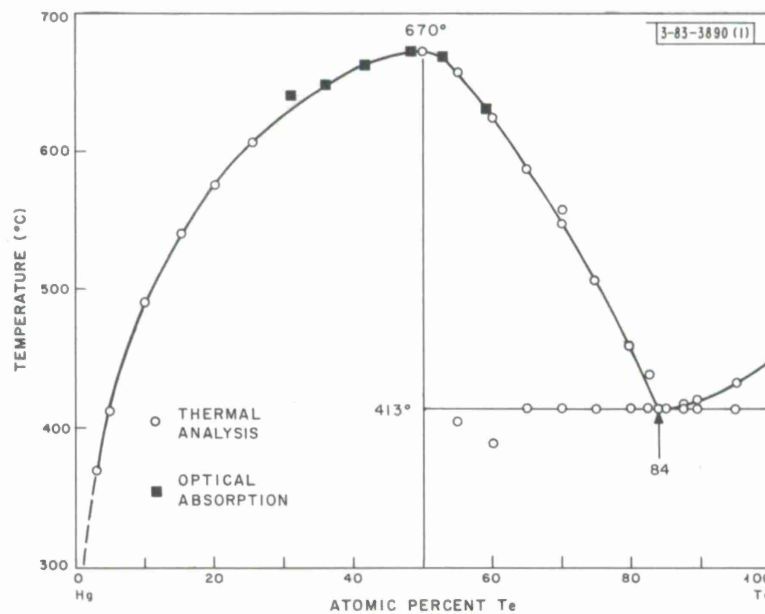


Fig. III-1. Phase diagram of Hg-Te system.

The melting point of HgTe measured in the present investigation is 670°C, the same value reported by Delves and Lewis.<sup>2</sup> The temperature and composition of the eutectic between HgTe and tellurium are  $413.5 \pm 0.5^\circ\text{C}$  and 84 atomic-percent tellurium, respectively, in comparison with the respective values of  $411 \pm 3^\circ\text{C}$  and 88 atomic-percent tellurium reported by Pellini and Aureggi<sup>3</sup> in 1910. For samples containing 80 or more atomic-percent tellurium, the liquidus points of Pellini and Aureggi are in good agreement with the present values. For lower percentages of tellurium, their temperatures are systematically lower than the present ones, probably due to the loss of mercury from their samples by preferential vaporization. For 66 atomic-percent tellurium, the lowest tellurium content they studied, their liquidus temperature is 548°C, compared with the present value of 583°C.

Delves<sup>4</sup> has reported a region of two immiscible liquid phases in the vicinity of 53 to 56 atomic-percent tellurium, with a monotectic temperature of  $664 \pm 2^\circ\text{C}$ . The present data do

### Section III

not confirm the existence of a two-liquid-phase region in this location, since initial liquidus arrests were observed at 661° and 656°C, respectively, in cooling runs on samples with nominal compositions of 54.2 and 55.0 atomic-percent tellurium. (The actual melt compositions at the liquidus temperatures are estimated to be 54.4 and 55.2 atomic-percent tellurium, respectively, because of preferential vaporization of mercury.) According to Delves' results, monotectic arrests at  $664 \pm 2^\circ\text{C}$  should have been observed in both runs.

A.J. Strauss  
R.F. Brebrick

#### B. PRESSURES OF Hg AND Se IN EQUILIBRIUM WITH HgSe(c)

In order to determine the pressures of mercury and selenium in the vapor over Hg-saturated, Se-saturated, and congruently subliming HgSe(c) between 450° and 800°C, the optical absorption of the vapor maintained at 860°C has been measured between 2000 and 7000 Å.<sup>5</sup> In agreement with mass spectrographic results, no evidence for the species HgSe(g) was found, and accordingly the optical density was assumed to be the sum of the densities due to mercury and selenium vapors. The partial pressure of mercury,  $p_{\text{Hg}}$ , and the sum of the partial pressures of all selenium species,  $p_{\Sigma}$ , could therefore be obtained from the measured densities together with calibration data for pure mercury<sup>1</sup> and pure selenium.<sup>6</sup>

The values of  $p_{\text{Hg}}$  and  $p_{\Sigma}$  along the three-phase lines for Hg-saturated and Se-saturated HgSe(c) are plotted against  $1/T$  in Fig. III-2. Where measured values (solid lines) could not be

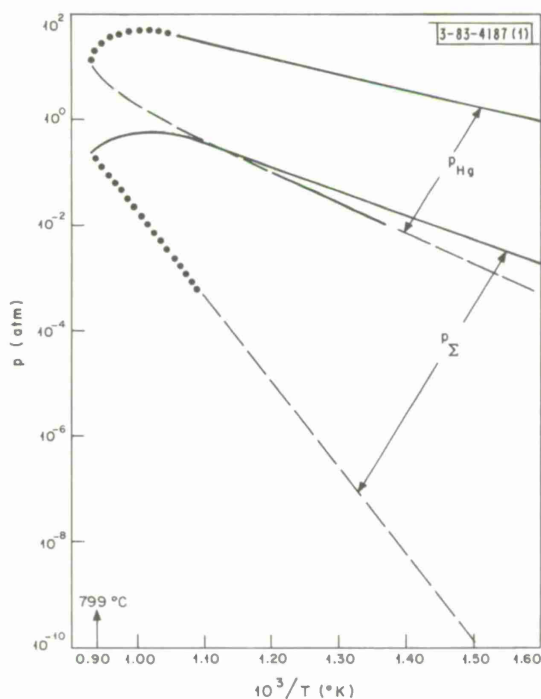


Fig. III-2. Partial pressure of Hg(g),  $p_{\text{Hg}}$ , and sum of partial pressures of all selenium species,  $p_{\Sigma}$ , along three-phase lines for Hg- and Se-saturated HgSe(c).

obtained, the plot gives calculated values (dashed lines), determined for one component from the measured values for the other, or estimated values (dotted lines). Analysis of the data shows that Hg-saturated HgSe(c) is in equilibrium with essentially pure Hg( $\ell$ ) up to 659°C and contains at least 48.5 atomic-percent selenium. The maximum value of  $p_{\text{Hg}}$  over HgSe(c) is estimated to be about 50 atm. The maximum value of  $p_{\Sigma}$  is 0.62 atm, the pressure over Se-saturated HgSe(c) near 722°C.

Values of  $p_{\text{Hg}}$  and  $p_{\Sigma}$  in equilibrium with congruently subliming HgSe(c) were measured between about 450° and 600°C. The data are well represented by the expressions  $\log p_{\text{Hg}}(\text{atm}) = -5.90(10^3)/T + 6.22$  and  $\log p_{\Sigma}(\text{atm}) = -6.04(10^3)/T + 5.82$ . The experimental values of  $p_{\text{Hg}}$  agree closely with those calculated from the measured values of  $p_{\Sigma}$  by applying the condition that the atom fractions of mercury and selenium in the congruently subliming vapor are essentially equal and using the published<sup>7</sup> equilibrium constants for the dissociation of  $\text{Se}_4(\text{g})$ ,  $\text{Se}_6(\text{g})$ , and  $\text{Se}_8(\text{g})$  into  $\text{Se}_2(\text{g})$ .

Since both  $p_{\text{Hg}}$  and  $p_{\Sigma}$  were measured for congruently subliming and Se-saturated HgSe(c), these data could be used to calculate the standard Gibbs free energy of formation of HgSe(c) according to the expression  $\Delta G_f^{\circ}[\text{Hg}(\text{g}) + 1/2 \text{Se}_2(\text{g}) = \text{HgSe}(\text{c})] = RT \ln p_{\text{Hg}} p_2^{1/2}$ . The values of  $p_2$ , the partial pressure of  $\text{Se}_2(\text{g})$ , were calculated from the measured values of  $p_{\Sigma}$  by using the published<sup>7</sup> equilibrium constants for Se vapor. The values of  $\Delta G_f^{\circ}$  obtained for congruently subliming and Se-saturated HgSe(c) are the same within the limits of experimental error. Taking the average gives  $\Delta G_f^{\circ} = -41.92 + 42.40(10^{-3}) T$  kcal/mole between about 450° and 600°C. These are the first values which have been reported for the free energy of formation of HgSe(c). Values of  $\Delta H_f^{\circ} = -10.8$  kcal/mole and  $\Delta S_f^{\circ} = -4.99$  eu/mole are obtained for the formation of HgSe(c) from Hg( $\ell$ ) and Se(c), all at 300°K, by extrapolating the free energy expression and using published thermodynamic data for HgSe(c), Hg(g,  $\ell$ ), and Se(g,  $\ell$ , c).

R.F. Brebrick

### C. THERMODYNAMIC STUDIES OF InTe PRESSURE-TEMPERATURE DIAGRAM

The pressure-temperature diagram for InTe has been reported previously.<sup>8</sup> The pressure at which the low-pressure phase, InTe (I), is transformed into the high-pressure phase, InTe (II), decreases with increasing temperature. The melting point of InTe (II) increases with increasing pressure. The melting curve of InTe (I) and the precise location of the InTe (I)-InTe (II)-InTe (liquid) triple point could not be determined. It was found that at sufficiently low temperatures InTe (II) can be retained at atmospheric pressure as a metastable phase.

As an extension of the pressure-temperature studies, two properties of InTe have been measured at atmospheric pressure:  $\Delta V_f$ , the change in volume of InTe (I) on melting, and  $\Delta H_t$ , the heat of transformation of metastable InTe (II) into InTe (I). These quantities are related to the slopes of the melting curve of InTe (I) and of the phase boundary between InTe (I) and InTe (II), respectively, by the Clausius-Clapeyron equation:  $dT/dP = T\Delta V/\Delta H$ , where  $T$  is the absolute temperature of the phase transition,  $P$  is the pressure,  $\Delta V$  is the change in volume, and  $\Delta H$  is the heat of transition.

The value of  $\Delta V_f$  for InTe (I) at 696°C and 1 atm was determined by the method of fed and unfed castings, as modified by Ball.<sup>9</sup> The densities found by this method for solid and liquid InTe at the melting point are, respectively,  $5.845 \pm 0.081$  g/cm<sup>3</sup> (average of six determinations)

Section III

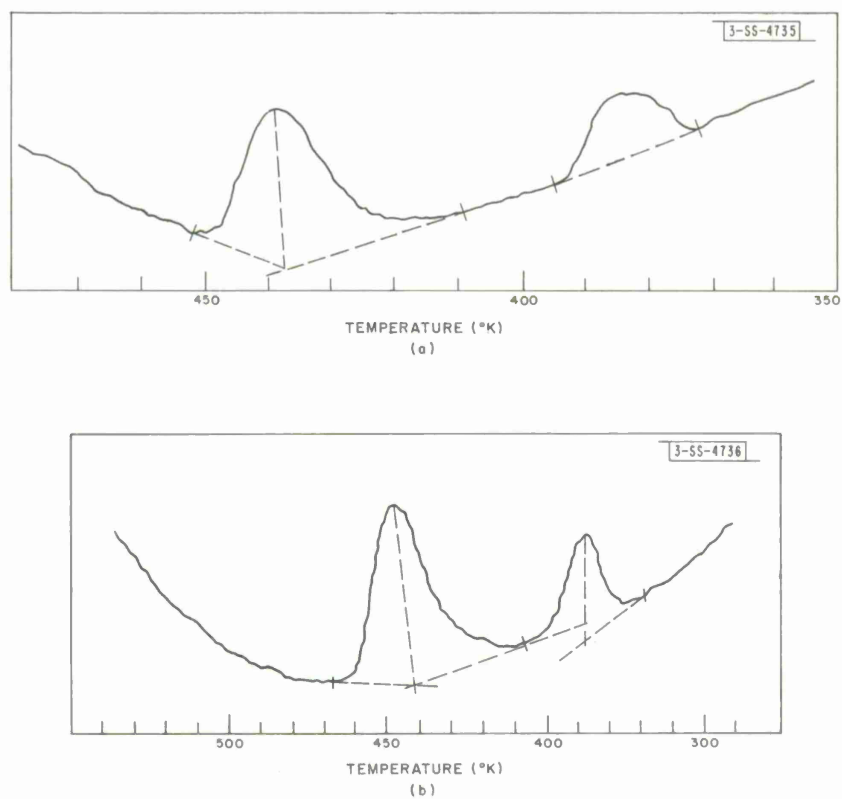


Fig. III-3. Recorder traces obtained during two differential-scanning calorimeter runs in which high-pressure form of InTe, InTe (II), was transformed into low-pressure form, InTe (I). Abscissa and ordinate give temperature in degrees Kelvin and power in arbitrary units, respectively. Dashed lines are estimated base lines used in determining areas under power peaks. (a) Heating rate: 20 deg/minute. (b) Heating rate: 40 deg/minute.

and  $5.733 \pm 0.033 \text{ g/cm}^3$  (average of seven determinations). The corresponding molar volumes are  $41.48 \pm 0.44$  and  $42.28 \pm 0.27 \text{ cm}^3/\text{mole}$ , respectively, and the value of  $\Delta V_f$  is therefore  $0.80 \pm 0.72 \text{ cm}^3/\text{mole}$ . Substituting this value for  $\Delta V_f$  and the measured<sup>10</sup> value of  $4.29 \text{ kcal/g-atom}$  for  $\Delta H_f$  into the Clausius-Clapeyron equation gives  $dT_f/dP = 2.16 \text{ deg/kbar}$  as the initial slope of the melting curve for InTe (I). If this slope does not change with pressure up to the triple point, the InTe (I) melting curve intersects the InTe (I)-InTe (II) phase boundary at 11 kbar and  $718^\circ\text{C}$ . This location for the triple point is close to the one estimated previously.<sup>8</sup>

Values of  $\Delta H_t$  for the InTe (II)  $\rightarrow$  InTe (I) transition at atmospheric pressure were obtained by both metal-solution and differential-scanning calorimetry. The first method was used to determine  $\Delta H_t$  at  $0^\circ\text{C}$  by comparing the temperature changes which occurred when samples of InTe (I) and InTe (II) initially at  $0^\circ\text{C}$  were separately dissolved in molten bismuth initially at  $350^\circ\text{C}$ . The final concentrations of indium and tellurium in the bismuth bath were kept below 2 atomic-percent so that the calculations could be made for the case of infinite dilution. The calorimeter was calibrated by adding bismuth initially at  $0^\circ\text{C}$  to the bismuth bath. Details of the experimental technique and calculation procedure are given elsewhere.<sup>11</sup> The value of  $\Delta H_t$  found by this method is  $0.44 \pm 0.01 \text{ kcal/g-atom}$ .

The value of  $\Delta H_t$  was also determined with a differential-scanning calorimeter (Perkin-Elmer Model DSC-1). In this apparatus the sample and an inert standard, which are sealed into separate aluminum-foil capsules, are heated at a constant rate by independent resistance heaters. The differences in heater power required to keep the sample and standard temperatures equal throughout the run are recorded as a function of temperature. When one stable phase is transformed into another, a peak appears on the recorder chart at the transformation temperature, and the area under the peak is proportional to  $\Delta H_t$ . Although there is no thermodynamically defined temperature for the transformation of a metastable to a stable phase,  $\Delta H_t$  for such a transition can also be measured by scanning calorimetry if the rate of transformation is strongly temperature dependent. In that event, for sufficiently rapid heating rates the transformation occurs predominantly within a narrow temperature range and produces a well-defined exothermic peak. In the present experiments, two such peaks were observed in each run, as seen in the typical recorder traces shown in Figs. III-3 (a-b). These traces were obtained for heating rates of 20 and 40 deg/minute, respectively.

The existence of two exothermic peaks indicates that the InTe (II)  $\rightarrow$  InTe (I) transformation takes place in two steps, and therefore confirms the finding of Sclar, Carrison, and Schwartz<sup>12</sup> that at atmospheric pressure an intermediate phase, InTe (II)', is formed during the transformation. In eight runs, the temperatures at which the evolution of heat was first detected were  $94 \pm 6^\circ\text{C}$  for the first peak and  $134 \pm 6^\circ\text{C}$  for the second peak. These values are consistent with the results which Sclar, *et al.*,<sup>12</sup> obtained in their x-ray and metallographic studies. The relative quantities of heat liberated during the two steps differed considerably from run to run. The percentage of the total evolved during the first step ranged from 14 to 39 percent. However, the total heat liberated during the two steps was quite reproducible. The average value obtained for  $\Delta H_t$  is  $0.42 \pm 0.03 \text{ kcal/g-atom}$ , in excellent agreement with the result found by metal-solution calorimetry.

The value of  $\Delta H_t$  for the InTe (II)  $\rightarrow$  InTe (I) transformation at room temperature and 30 kbar can be calculated according to the Clausius-Clapeyron equation from the measured<sup>8</sup> slope of the

Section III

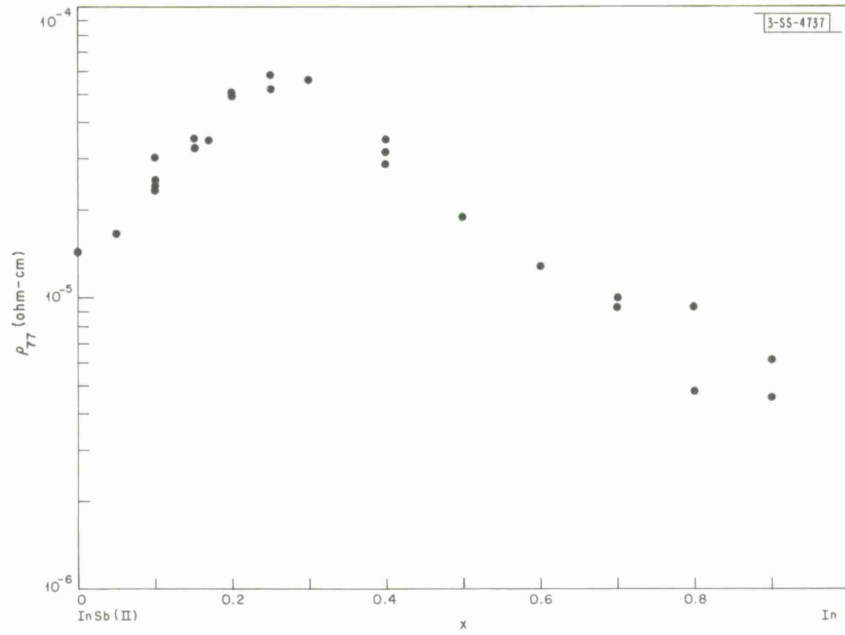


Fig. III-4. Resistivity at 77°K ( $\rho_{77}$ ) vs composition for the high-pressure InSb-In system. Composition parameter is  $x$  in formula  $\text{InSb(II)}_{1-x}(\text{2 In})_x$ .

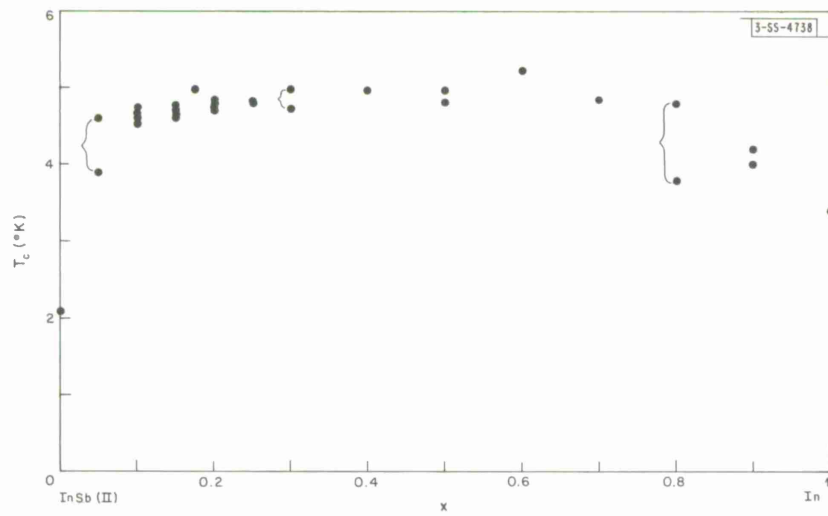


Fig. III-5. Superconducting transition temperature ( $T_c$ ) vs composition for high-pressure InSb-In system. Where there are two bracketed points, two discrete transitions were observed.

InTe (I)-InTe (II) phase boundary and the value of  $\Delta V_t$  obtained from the x-ray densities of the two phases at atmospheric pressure and their compressibilities<sup>13</sup> between 1 atm and 30 kbar. The calculated value of  $\Delta H_t$  is 0.21 kcal/g-atom, only about half the calorimetric value for 1 atm. The difference indicates that the average pressure coefficient of heat content is greater for InTe (I) than for InTe (II) by about  $8 \times 10^{-6}$  kcal/(g-atom)-atm between 1 atm and 30 kbar.

M. D. Banus  
P. M. Robinson†

#### D. HIGH-PRESSURE InSb-In SYSTEM

Additional samples of nominal composition  $\text{InSb(II)}_{1-x}(\text{2 In})_x$  have been prepared in order to extend the previous investigation<sup>14</sup> of the high-pressure InSb-In system over the entire range from pure InSb (II), the high-pressure phase of InSb, to pure indium. The new samples were produced at 37 kbar, cooled to about 150°K before releasing the pressure, and stored at 77°K, as described previously,<sup>14</sup> in order to retain the high-pressure phase(s) at atmospheric pressure.

Resistivity at 77°K and superconducting transition temperature of all the samples are plotted against composition in Figs. III-4 and III-5, respectively. With increasing indium content, the resistivity increases to a maximum at about  $x = 0.3$  and then decreases smoothly to the value for pure indium. The transition temperature initially increases sharply from the value of 2.1°K for pure InSb (II), remains essentially constant between 4.5° and 5.0°K from  $x = 0.1$  to  $x = 0.7$ , and then decreases to the value for pure indium.

It was reported previously<sup>14</sup> that the amount of heat liberated when a high-pressure sample is transformed into the atmospheric pressure form is much larger for  $x = 0.2$  than for  $x = 0.15$  or below. This conclusion was based on time-temperature data obtained in drift runs during which samples were heated slowly from 77°K through the temperature at which they were rapidly transformed to the stable form. In additional drift runs, it has been found that the amount of heat liberated remains relatively high between  $x = 0.2$  and  $x = 0.5$ , but is much lower for  $x = 0.6$  or above. We conclude from this result that there is a phase in the high-pressure InSb-In system which differs in structure from both InSb (II) and indium. This phase apparently lies between  $x = 0.2$  and  $x = 0.5$ , but its exact composition cannot be determined from the thermal data.

M. D. Banus  
Lynne B. Farrell  
A. J. Strauss

#### E. PRESSURE DEPENDENCE OF B8 $\approx$ B31 TRANSITION TEMPERATURE IN MnAs

Under atmospheric pressure, MnAs is transformed at 44°C from the low-temperature phase with B8 structure to the high-temperature B31 phase. Pressure dependence of the transition temperature has been determined by measuring the change of resistance with hydrostatic pressure at various fixed temperatures between 25° and -72°C. The experimental technique has been described previously.<sup>15</sup> Results of the measurements are shown in Fig. III-6. The equation of the curve drawn through the data points is  $P^* = -5.6230 + 0.1073 T - 0.000283 T^2$ , where  $P^*$  is the pressure in kilobars and  $T$  is the transition temperature in degrees Kelvin. The form

† Department of Metallurgy, M.I.T.

Section III

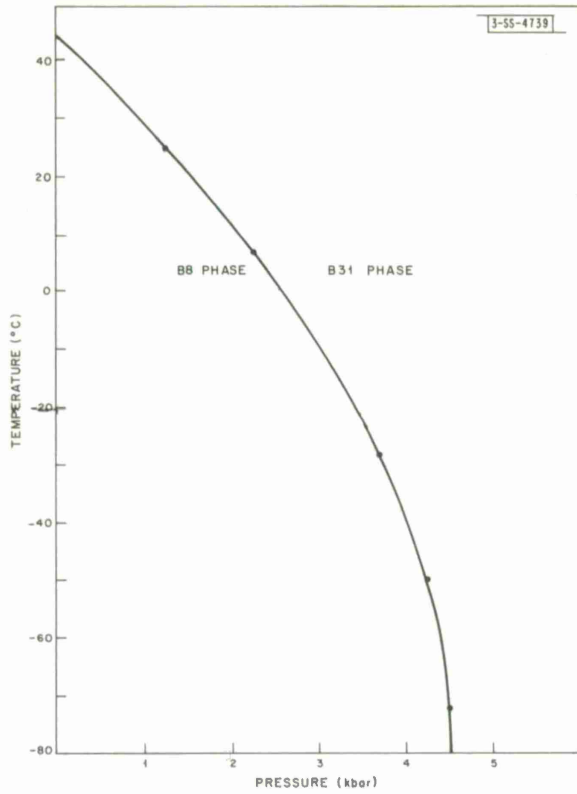


Fig. III-6. Pressure dependence of B8  $\rightleftharpoons$  B31 transition temperature in MnAs.

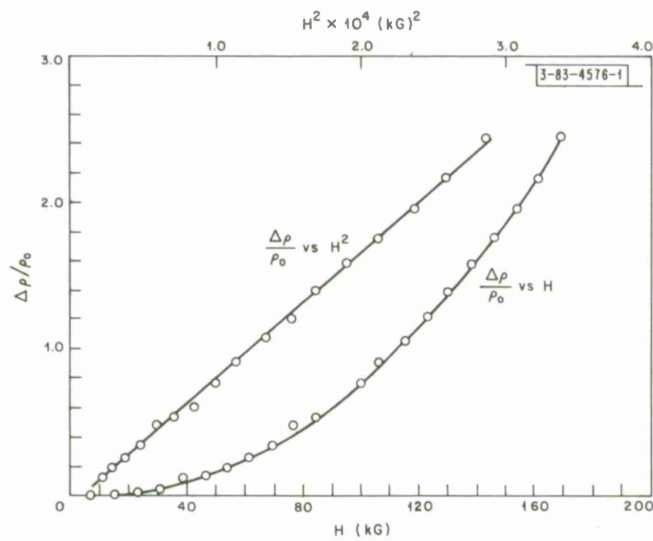


Fig. III-7. Magnetoresistance ( $\Delta\rho/\rho_0$ ) of  $\text{Ti}_2\text{O}_3$  as a function of magnetic field (H) and of  $H^2$ . Current axis is tilted  $45^\circ$  away from c-axis toward a-axis. Measurements made at  $4.2^\circ\text{K}$ .

of this equation suggests that there is a critical pressure of about 4.5 kbar, above which the B31 phase is stable at all temperatures.

J. A. Kafalas  
W. A. Newman  
J. B. Goodenough

#### F. ELECTRICAL PROPERTIES OF $Ti_2O_3$

Electrical measurements have been made on  $Ti_2O_3$  single crystals containing considerably less nitrogen, the principal impurity, than earlier samples. Reduction in nitrogen content has been achieved by using higher-purity titanium metal in preparing the oxide and by using hot titanium as a getter to purify the argon used as a protective atmosphere in synthesis and crystal growth. In contrast to previous results,<sup>16</sup> both the resistivity ( $\rho$ ) and Hall coefficient depend strongly on crystal orientation, and  $\rho$  now increases roughly exponentially with decreasing temperature.

Magnetoresistance,  $\Delta\rho/\rho_0$ , has been measured at 4.2°K on a single crystal whose c-axis is oriented at 45° with respect to the current direction. As shown in Fig. III-7,  $\Delta\rho/\rho_0$  is proportional to the square of the magnetic field up to 170 kG, the highest field employed. The value of  $\Delta\rho/\rho_0$  at 170 kG is 2.5, compared with the previous maximum value of 0.12 for  $Ti_2O_3$  at 100 kG. The value of 2.5 is too high to be explained in terms of a one-band model for the transport properties.

J. M. Honig

#### G. THEORY: LOCALIZED VS COLLECTIVE ELECTRONS IN TRANSITION-METAL COMPOUNDS

There are two limiting theories for the description of outer electrons in solids: a localized-electron (crystal-field) theory and a collective-electron (band) theory. Whereas f-electrons are always localized and outer s- and p-electrons are almost always collective, the outer d-electrons are localized in some crystals, collective in others, and in some, localized and collective d-electrons are simultaneously present. Spontaneous crystallographic distortions of transition-metal compounds from a higher to a lower symmetry phase can provide an operational criterion for distinguishing whether the outer d-electrons are localized, are band electrons as a result of cation-cation interactions, or are band electrons as a result of cation-anion covalence.

By using this criterion, it is possible to show that the outer d-electrons in CrS are localized, but that in FeS the outer d-electron of antiparallel spin is collective, belonging to the cation sublattice as a whole at high temperatures and to molecular clusters at low temperatures. The TiP and NbAs structures illustrate changes in translational symmetry that circumscribe the Fermi surface of cation-sublattice band electrons with a Brillouin-zone surface. Distortions from NiAs to MnP structure appear to be induced by cation-anion bonding, cation-cation interactions contributing only via the introduction of an anisotropic elastic restoring force.

J. B. Goodenough

#### H. WET CHEMICAL ANALYSIS

##### 1. Lanthanum and Yttrium Cobalt Oxides

A complexometric method accurate to three parts per thousand has been developed for the analysis of lanthanum and yttrium cobalt oxides. The samples are usually dissolved in 1:2  $HNO_3$ ,

## Section II:

but occasionally it is necessary to fuse the sample in  $K_2S_2O_7$  and dissolve the fusion in 10%  $H_2SO_4$ .

The total rare earth plus cobalt is determined on an aliquot containing about 10 mg of sample. The aliquot is buffered with  $NH_4NO_3-NH_4OH$  to a pH between 8.3 and 8.6, excess EDTA is added, and the excess is titrated with standard copper solution to a potentiometric end point using the Reilley gold-amalgam electrode.<sup>17</sup>

The rare earth alone is determined on an aliquot containing about 5 mg of the rare earth. The aliquot is buffered as for the above determination, the solution cooled in an ice bath, and 5% KCN solution added to complex the cobalt. After two minutes, excess EDTA is added. Excess  $CN^-$  is then removed by adding formaldehyde dropwise and excess EDTA is titrated to a potentiometric end point using the gold-amalgam electrode. Automatic titration equipment is used for both titrations of excess EDTA.

### 2. Iron-Nickel-Copper Alloy Thin Films

A method has been developed for the analysis of iron-nickel-copper alloy thin films. Samples of 1 to 2 mg are dissolved in 10%  $HNO_3$ . Iron is determined on an aliquot containing about 0.2 mg Fe by the ortho-phenanthroline spectrophotometric method. Nickel interference, which occurs when  $Ni/Fe > 4$ , is eliminated by using a large excess of ortho-phenanthroline and by making the photometric measurement immediately after the ortho-phenanthroline addition. The spectrophotometric measurements are made in a 1-cm cell at 495 m $\mu$ . Beer's law is obeyed for solutions containing 0.4 to 4.0  $\mu g$  Fe per milliliter. The method is accurate to about three parts per thousand.

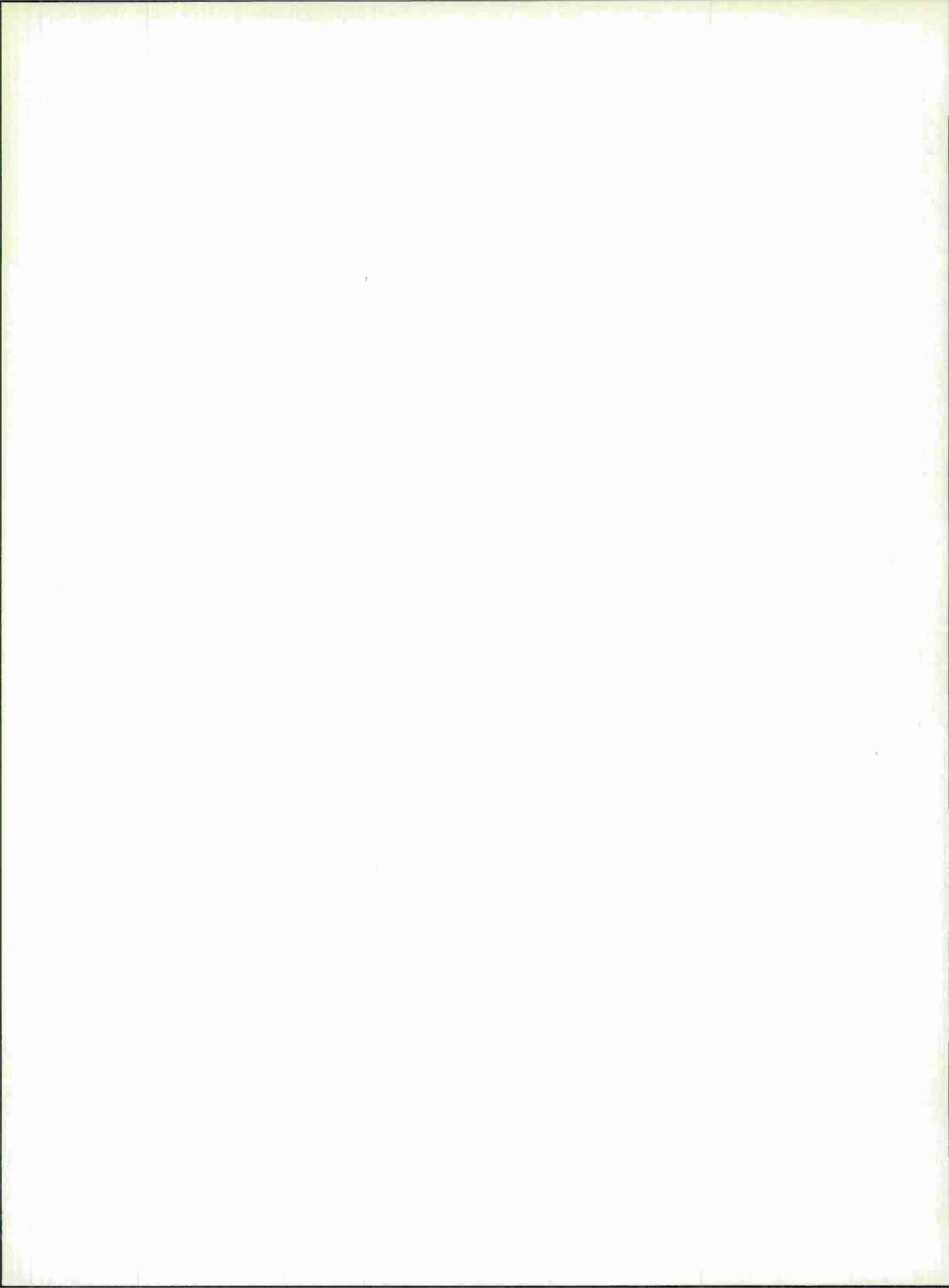
Nickel is determined by the usual dimethylglyoxime spectrophotometric method. Citric acid is added to eliminate the interferences. Iodine and dimethylglyoxime are then added to develop the color, which is measured after 10 minutes in a 5-cm cell at 535 m $\mu$ . Beer's law is obeyed for solutions containing 0.4 to 2.0  $\mu g$  Ni per milliliter. The method is accurate to about three parts per thousand.

Copper is determined on an aliquot containing 0.4 to 2.0  $\mu g$  Cu. Citric acid and EDTA are added to eliminate the interferences, the pH is adjusted to 8.5 to 9.0, and sodium diethyl-dithiocarbamate is added to the solution. The resulting Cu complex is extracted in  $CCl_4$ , and the absorbance of the  $CCl_4$  solution is measured in a 1-cm cell at 430 m $\mu$ . As suggested by Sandell<sup>18</sup> and by Snell, Snell, and Snell,<sup>19</sup> the aqueous sodium diethyl-dithiocarbamate is stored in amber glass in the dark until use, and the sample solutions are protected from strong light after the color complex is formed. This system does not obey Beer's law. About 1-percent accuracy is achieved.

E. B. Owens  
J. C. Cornwell

## REFERENCES

1. R. F. Brebrick and A. J. Strauss, *J. Phys. Chem. Solids* 26, 989 (1965).
2. R. T. Delves and B. Lewis, *J. Phys. Chem. Solids* 24, 549 (1963).
3. M. Hansen and K. Anderko, *Constitution of Binary Alloys* (McGraw-Hill, New York, 1958), 2nd ed., p. 840.
4. R. T. Delves, *Brit. J. Appl. Phys.* 16, 343 (1965).
5. R. F. Brebrick, *J. Chem. Phys.* 43, 3846 (1965).
6. \_\_\_\_\_, *J. Chem. Phys.* (in press); Solid State Research Report, Lincoln Laboratory, M. I. T. (1965:2), p. 36, DDC 624611.
7. V. V. Illarionov and L. M. Lapina, *Doklady Akad. Nauk S. S. S. R.* 114, 1021 (1957).
8. M. D. Banus, R. E. Hanneman, K. Goosen, and M. Strongin, *Science* 142, 662 (1963).
9. D. L. Ball, *J. Chem. Eng. Data* 8, 61 (1963).
10. P. M. Robinson and M. B. Bever, *Trans. Met. Soc. AIME* (in press).
11. B. W. Howlett, J. S. D. Leach, L. B. Tickmar, and M. B. Bever, *Rev. Sci. Instr.* 33, 619 (1962).
12. C. B. Sclar, L. C. Carrison, and C. M. Schwartz, *Science* 147, 1569 (1965).
13. A. J. Darnell and W. F. Libby, *Phys. Rev.* 135, A1453 (1964).
14. Solid State Research Report, Lincoln Laboratory, M. I. T. (1965:2), p. 40, DDC 624611.
15. *Ibid.* (1965:1), p. 50, DDC 622446, H-678.
16. *Ibid.* (1965:2), p. 37, DDC 624611.
17. C. N. Reilley, R. W. Schmidt, and D. W. Lamson, *Anal. Chem.* 30, 953 (1958).
18. E. B. Sandell, *Colorimetric Determination of Traces of Metals* (Interscience, New York, 1959), p. 437.
19. F. D. Snell, C. T. Snell, and C. A. Snell, *Colorimetric Methods of Analysis* (Van Nostrand, New York, 1959), p. 46.



## IV. PHYSICS OF SOLIDS

### A. ELECTRONIC BAND STRUCTURE

#### 1. Reflectivity of $\text{ReO}_3$

In the last Solid State Research Report (1965:2), measurements on the reflectivity of  $\text{ReO}_3$  were reported in the photon energy range of 0.2 to 3.8 eV. These measurements have been extended to 12 eV, using a vacuum ultraviolet monochromator. The results at room temperature are shown in Fig. IV-1. The curve shows a Drude-like form at energies less than 2 eV and peaks at 4.6 and 9.6 eV due to interband contributions. By approximating the reflectivity for low (<0.2 eV) and high (>12.0 eV) regions, the optical constants,  $n$  and  $k$ , and the dielectric constants,  $\epsilon_1$  and  $\epsilon_2$ , can be obtained from a Kramers-Kronig analysis of the reflectivity data. In theory, the dielectric constant  $\epsilon = \epsilon_1 + i\epsilon_2$  can be separated into its Drude free-electron parts  $\epsilon_1^f$  and  $\epsilon_2^f$  and its bound-electron parts  $\epsilon_1^b$  and  $\epsilon_2^b$  where

$$\begin{aligned}\epsilon_1 &= \epsilon_1^f + \epsilon_1^b \\ \epsilon_2 &= \epsilon_2^f + \epsilon_2^b\end{aligned}\tag{1}$$

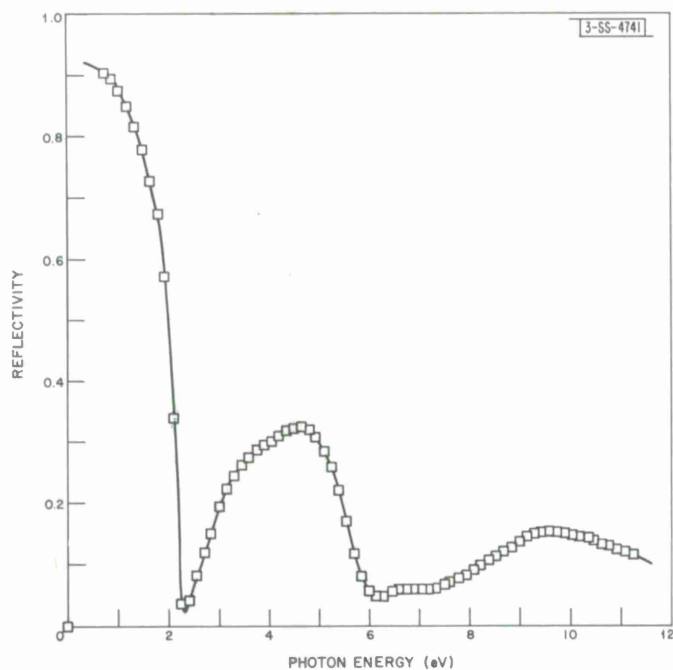


Fig. IV-1. Reflectivity of  $\text{ReO}_3$  at room temperature.

## Section IV

and  $\epsilon_1^f$  and  $\epsilon_2^f$  have the form

$$\begin{aligned}\epsilon_1^f &= 1 - \frac{\omega_{pa}^2}{\omega^2 + \gamma^2} \\ \epsilon_2^f &= \frac{\omega_{pa}^2 \gamma}{\omega(\omega^2 + \gamma^2)}\end{aligned}\quad (2)$$

Here  $\omega_{pa}^2 = 4\pi Ne^2/m^*$  and  $\gamma$  is the relaxation frequency which is not necessarily a constant.

At the present time, various techniques are being used to separate the dielectric constants  $\epsilon_1$  and  $\epsilon_2$  obtained from the Kramers-Kronig analysis into free- and bound-electron parts in order to evaluate such parameters as  $m^*$  and  $\gamma$  which may be compared with DC conductivity measurements. An attempt will also be made to interpret, from energy band theory considerations, the origin of the interband transitions above 2 eV.

W. J. Scouler    A. Ferretti  
J. Feinleib     B. Feldman

### 2. Band Structure of $\text{ReO}_3$

The simplified LCAO<sup>1</sup> (linear combination of atomic orbitals) or tight binding scheme has been used to investigate the band structure of  $\text{ReO}_3$ . The study illustrates the connection between ligand field theory and energy band theory, and indicates the range of validity of the former model for this compound. Using a linear combination of rhenium 6s-, 6p-, and 5d-orbitals and of oxygen 2s- and 2p-orbitals, the  $21 \times 21$  secular determinant was solved analytically under certain simplifying assumptions. In conformity with the scheme proposed by Goodenough,<sup>2</sup> the energy levels were found to separate into  $\sigma$  and  $\pi$  bonding and antibonding bands and into a set of nonbonding  $\pi$  levels made up of oxygen p-orbitals. Analytic expressions have been found for the structure of the antibonding  $\pi$  band in which the Fermi level of  $\text{ReO}_3$  is situated. In order to obtain a quantitative description of the energy bands, estimates of the various parameters which occur in the simplified LCAO scheme must be made. This is being accomplished by using the augmented plane-wave (APW) method of Slater<sup>3</sup> to fit these bands to electronic energy values calculated at symmetry points  $\Gamma$  and X, and along  $\Delta$ , the line joining these points. This permits detailed predictions concerning the magnetic and transport properties of  $\text{ReO}_3$ .

J. M. Honig  
J. O. Dimmock

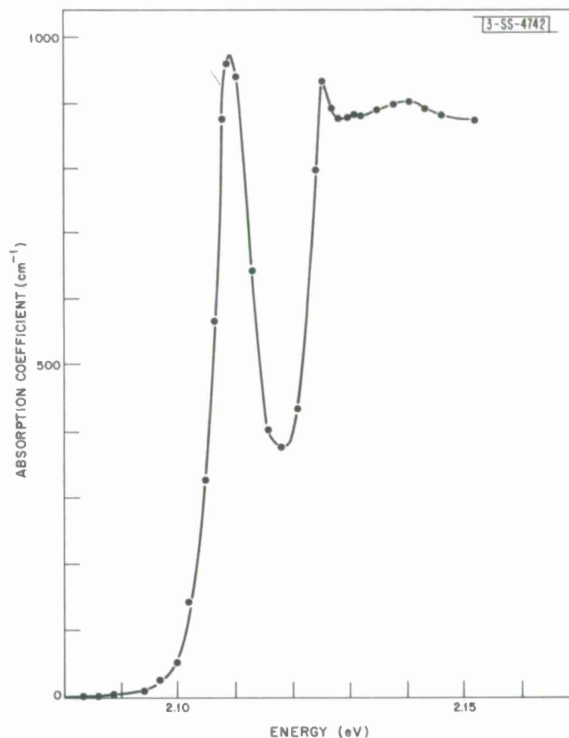
### 3. Magnetoabsorption of Direct Transition in Gallium Selenide<sup>†</sup>

Investigation of the band structure of GaSe, by studying interband magneto-optical absorption, is being continued. Much more highly resolved data than that reported previously<sup>4</sup> have been obtained in the Faraday geometry. Preliminary results have also been obtained in the

<sup>†</sup> This experiment was conducted using the high field facilities of the National Magnet Laboratory, M.I.T.

Voigt configuration (magnetic field in the plane of the layers and the propagation vector of the radiation along the  $c$ -axis); the latter observations were made at  $1.5^\circ\text{K}$  and with magnetic fields of zero through  $90\text{ kG}$ .

Fig. IV-2. Optical absorption near direct edge in GaSe at  $1.5^\circ\text{K}$  with propagation vector  $\Gamma \parallel c$ -axis.



Samples have now been studied for which the zero-field data at  $1.5^\circ\text{K}$  show as many as three clearly defined exciton peaks in addition to the well-known broad absorption peak above the conduction band edge. A plot of the zero-field absorption constant as a function of energy for one of the better samples is given in Fig. IV-2. The binding energy of the exciton as determined from this series of lines is  $(21 \pm 1)\text{ meV}$ . Assuming that GaSe is essentially a three-dimensional material and using a dielectric constant of  $10.6$ , which is obtained from reflectivity data, one calculates a reduced effective mass  $m^* = 0.17 m$  from the observed exciton binding energy of  $21\text{ meV}$ .

A plot summarizing some of the more recent magnetoabsorption data taken in the Faraday geometry is shown in Fig. IV-3. The data shown are for left circularly polarized light; data taken for right circularly polarized light give a similar spectrum which is very slightly displaced to higher energies. The triangles represent data obtained by sweeping the wavelength at a fixed value of magnetic field; the crosses represent data obtained by sweeping the magnetic field at a fixed value of wavelength. Magnetic quantum numbers of the particular Landau sub-bands corresponding to the observed transitions have been identified and are indicated in the figure. The transitions themselves are all actually to exciton levels lying beneath these sub-bands. From the higher quantum number lines, a reduced effective mass of  $m^* = 0.14 m$  is obtained. From

Section IV

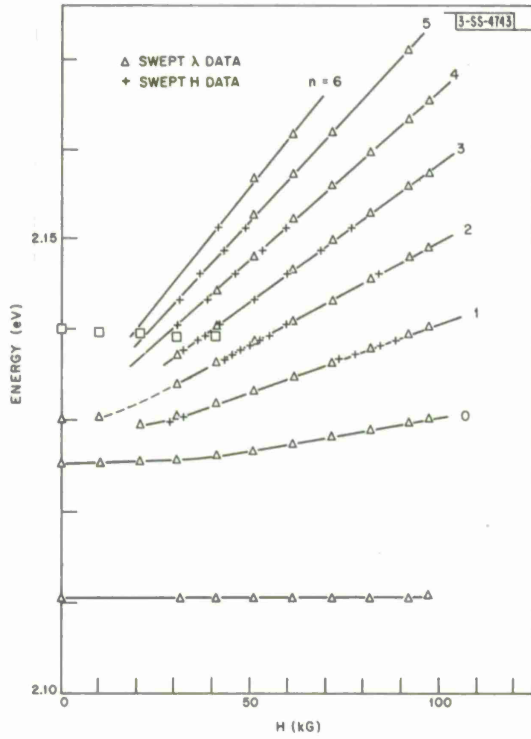
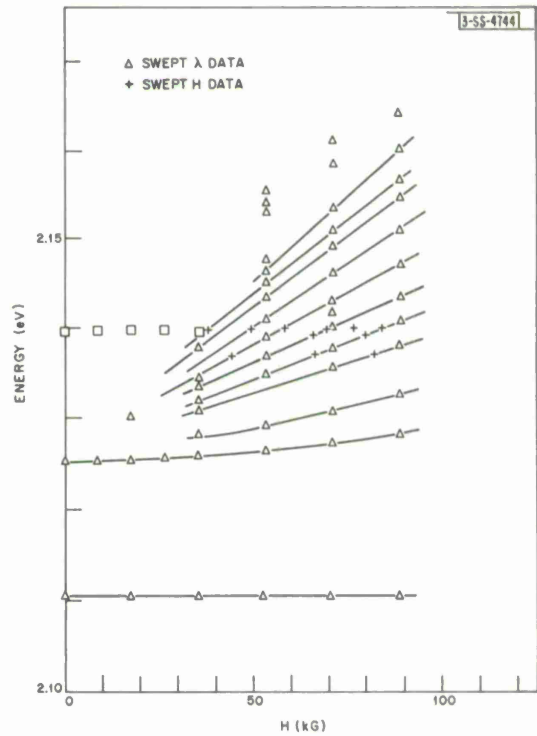


Fig. IV-3. Summary of magnetoabsorption results in GaSe at 1.5°K with magnetic field  $H \parallel \Gamma \parallel c$ -axis and left circular polarization. Spectrum for right circular polarization is slightly displaced and has been omitted for clarity.

Fig. IV-4. Summary of magnetoabsorption results in GaSe at 1.5°K with  $H \perp c$ -axis and  $\Gamma \parallel c$ -axis.



the convergence of the higher n-number "quasi-Landau level" lines, a zero-field edge energy of 2.130 eV and an exciton binding energy of  $\sim 20$  meV are obtained; this effective mass and binding energy is in agreement with the values obtained from the zero-field exciton spectrum.

The magnetoabsorption spectra in the Voigt configuration at 1.5 °K show oscillatory effects which are appreciably smaller in amplitude and more complex than those obtained in the Faraday geometry. A plot of the energies corresponding to the transmission minima as a function of magnetic field, as shown in Fig. IV-4, gives a collection of lines of nonuniform spacing and appears to indicate the presence of more than one series of transitions. In the present preliminary experiments in the Voigt geometry, we have not as yet carried out studies for different orientations of the magnetic field in the c-plane.

There are several models for the band structure of GaSe which are consistent with the present experimental data. The three most likely possibilities are (a) simple valence and conduction bands, both located at the  $\Gamma$ -point in the zone, (b) cigar-shaped ellipsoidal valence and conduction bands, located at the three equivalent vertices of the hexagonal Brillouin zone (Z-point), or (c) a cigar-shaped ellipsoid of revolution, located at  $\Gamma$ , for either the valence or conduction band and a more complex form for the remaining band.

J. Halpern

#### 4. Cyclotron Resonance in Gallium Selenide

Measurements of the microwave conductivity of GaSe as a function of magnetic field are being carried out with the hope of observing cyclotron resonance. This solid is of particular theoretical interest because of its layered structure. The large oscillatory magnetoabsorption effects obtained by Halpern (Sec. IV-A-3) on similar material indicate that the carrier relaxation times may be sufficiently long to resolve cyclotron resonance.

In the experiment, the sample is cemented to the bottom surface of a  $TM_{013}$  cylindrical cavity resonant at 70 GHz and cooled to 4.2 °K. The static magnetic field is applied in the plane perpendicular to the c-axis and is always perpendicular to the RF electric field. Carriers are excited by illuminating the sample with tungsten light chopped at 260 Hz and the signal reflected from the cavity is phase-sensitive detected at the same frequency.

Out of six samples examined so far, one has shown a well-resolved absorption peak at a field of 500 G, corresponding to an effective mass,  $m^* = 0.02 m$ , and with a line shape that indicates a value of approximately 1.5 for  $\omega\tau$ . No significant shift in the position of the peak is observed as the magnetic field is rotated in the plane perpendicular to the c-axis. Only one peak is observed in fields up to 25 kG and it is not known whether this corresponds to holes or electrons. Resonance with the magnetic field in a plane containing the c-axis has not yet been investigated.

Because the above result has been observed in one sample only, it must be regarded as preliminary and not conclusive. Efforts are continuing to observe effects in other samples.

S. Bermon  
W. C. Kernan

### 5. Magnetoplasma Cyclotron Resonance in p-Type Lead Selenide

Measurements of the microwave surface impedance at 70 GHz as a function of magnetic field of single crystal p-type PbSe with a carrier concentration of  $10^{18}$  holes/cm<sup>3</sup> are continuing. The conditions of the experiment are such that one does not expect to observe the usual cyclotron resonance, as for example in germanium, but resonances strongly affected by the high density plasma which exists in the solid.

In the present experiment the static magnetic field is in the plane of the sample surface which forms the central section of the bottom wall of a cylindrical cavity operating in the TE<sub>113</sub> mode. The sample surface itself must be of an extremely high quality, free from strain or damage, to satisfy the requirements on the relaxation time,  $\omega\tau > 1$ . A mica strip placed over the bottom surface, along a diameter of the cavity, removes the degeneracy of the cavity mode and allows the direction of the RF electric field to be fixed. Experiments are carried out at 4.2° and 1.2°K.

Absorption derivative curves in the range below 3 kG exhibit marked structure with very good repeatability. Using the classical skin effect theory and an infinite relaxation time, a preliminary theoretical analysis has been carried out for the data obtained with the static magnetic field aligned along the [100] and [110] axes, and with the ordinary and extraordinary modes of propagation in the crystal excited independently. Points of sharp descent are identified with dielectric anomalies. The behavior of the structure is consistent with that predicted by using the values of effective mass and anisotropy obtained from previous Shubnikov-de Haas measurements on this sample.<sup>5</sup> Azbel-Kaner-type resonance as an explanation for the main structure is ruled out. A more complete theoretical treatment which includes the effect of a finite relaxation time requires machine calculation. Such a program is currently under way.

Additional weak structure, which appears to resemble Shubnikov-de Haas oscillations, has also been observed at high magnetic fields. These effects are being examined further.

S. Bermon  
W. C. Kernan

### 6. Fourier Expansion for Energy Bands in a Periodic Solid

Electronic energy bands in solids are periodic in wave-vector space and hence are amenable to a Fourier expansion. The symmetry of the lattice and the degeneracies of the bands at high symmetry points in the Brillouin zone are included by using a generalization of the technique developed by Luttinger<sup>6</sup> for obtaining a Taylor's series expansion of the energy bands. The effective mass Hamiltonian thus derived is a matrix with dimension equal to the number of bands being considered. Experimentally observed quantities such as cyclotron effective masses, Fermi surface cross sections, de Haas-van Alphen periods, etc., are readily computed and thus can be used experimentally to determine the Fourier coefficients of the energy bands.

This technique is being applied to obtain, phenomenologically, the energy bands in the semi-metal antimony, where recent magnetoreflexion experiments<sup>7</sup> have given information about energy band gaps and effective masses at points L and T in the Brillouin zone. In order to establish the feasibility of such expansion in a metal, an application to aluminum is also being undertaken.

G. F. Dresselhaus  
Mildred S. Dresselhaus

## B. HYPERSONIC WAVES IN SOLIDS

### 1. Generation of Hypersonic Waves by Using Thin-Film CdS Transducers

Many of the difficulties and limitations arising from the excitation of hypersonic waves by surface effects, harmonic quartz transducers, or magnetostrictive films may be avoided by using vapor-deposited insulating films of piezoelectric materials. Consequently, an electron-beam technique, to be described in a later report, has been developed for the vapor deposition of insulating, piezoelectric thin-film CdS transducers onto various substrates.

The ideal CdS film would be a single hexagonal crystal with its *c*-axis perpendicular to the film surface. Then, by orienting the driving electric field with respect to the film surface, it would be possible to excite either longitudinal or transverse hypersonic waves; these waves could then be used as a probe to study certain properties of the substrate material.

To date, acoustically active CdS films have been deposited on single crystal specimens of aluminum, permalloy, indium antimonide, gallium arsenide, quartz, sapphire, and ruby. Pulse-echo techniques were used to determine whether or not a given film was acoustically active. The electromagnetic frequency range of excitation of the longitudinal mode in active films varied from 30.2 MHz for CdS on an aluminum substrate, to 70 GHz for CdS on a *z*-cut quartz rod (Sec. IV-B-2). The corresponding thickness range was from 70 to less than  $0.1\ \mu$ .

Whenever films thicker than one-half a wavelength have been deposited on quartz, transduction efficiency has improved as compared with surface generation in quartz alone. Figure IV-5(a) indicates the echo pattern obtained in the transverse mode at 1 GHz with a  $0.9\text{-}\mu$  film deposited on an *x*-cut quartz substrate. Figure IV-5(b) shows a similar pattern obtained at 1 GHz for the same substrate but without a film.

The patterns shown in Fig. IV-6(a) were obtained for propagation in the longitudinal mode at 1 GHz through *z*-cut quartz without a deposited film and those in Fig. IV-6(b) with a  $2.2\text{-}\mu$  film deposited on the same piece of quartz under identical conditions.

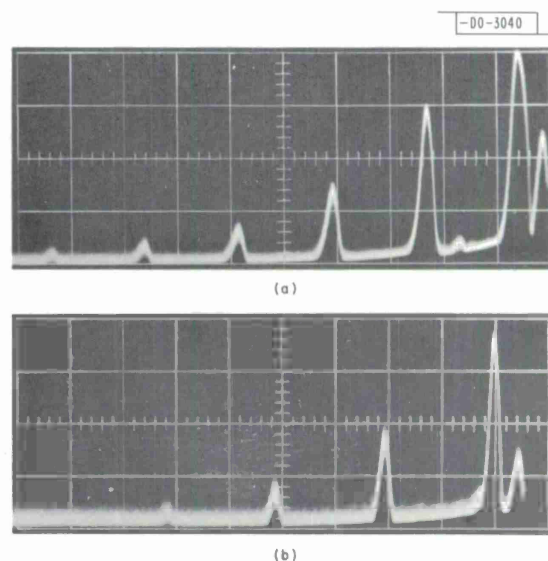


Fig. IV-5. Pulse-echo pattern of 1-GHz transverse waves in *x*-cut quartz at  $300^\circ\text{K}$ , (a) generated and detected by CdS transducer  $0.9\ \mu$  thick and (b) generated and detected by surface generation in quartz alone.

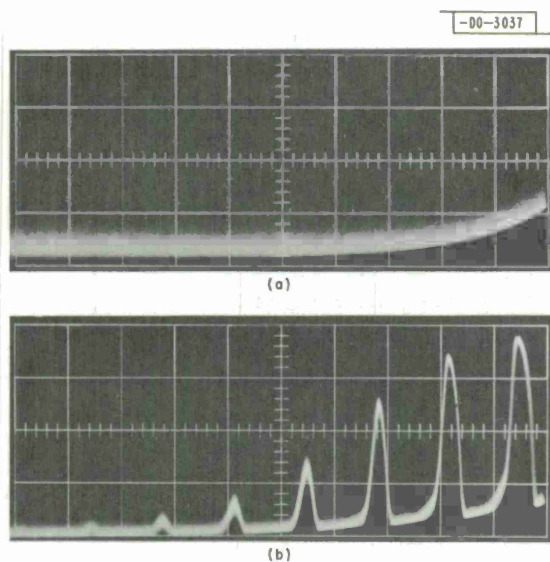


Fig. IV-6. (a) Expected result of attempt to excite 1-GHz longitudinal waves in z-cut quartz at room temperature by surface excitation of quartz. (b) Pulse-echo pattern of longitudinal waves in this same specimen of z-cut quartz under identical conditions but with vapor-deposited CdS transducer  $2.2\ \mu$  thick generating and detecting hypersonic waves.

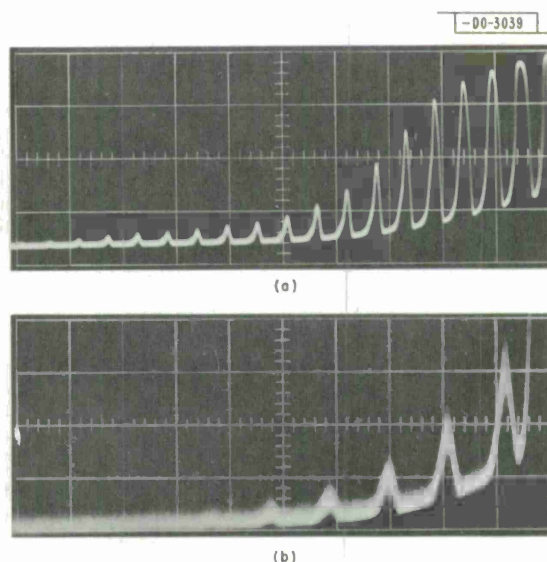


Fig. IV-7. Pulse-echo pattern of longitudinal waves in polycrystalline permalloy, (a) at 41 MHz and  $300^\circ\text{K}$ , generated and detected by vapor-deposited CdS transducer of thickness  $5.4\ \mu$  and (b) at 40.8 MHz and  $300^\circ\text{K}$ , with the waves generated and detected by resonant quartz plate bonded to sample and operating in its third harmonic.

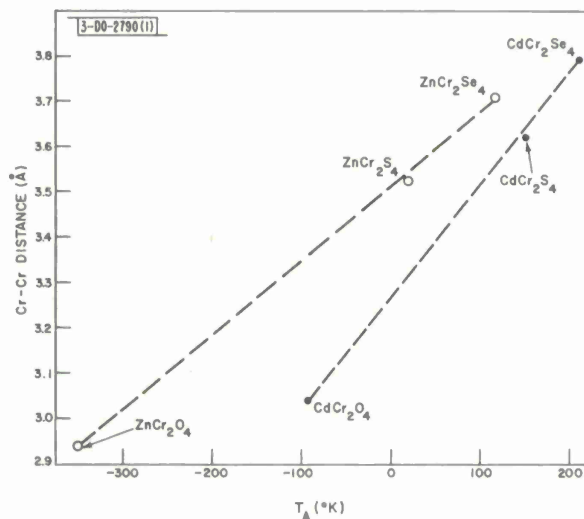


Fig. IV-8. Variation of asymptotic Curie temperature with  $\text{Cr}^{3+}$ - $\text{Cr}^{3+}$  separation.

Figure IV-7 shows the echo patterns for the longitudinal mode propagation in a permalloy sample, comparing a directly deposited CdS film, with a fundamental frequency at 41 MHz [Fig. IV-7(a)], to a resonant quartz plate transducer bonded to the same piece of permalloy and operating in its third harmonic at 40.8 MHz [Fig. IV-7(b)].

Immediate future plans call for measuring the transduction efficiency of CdS films as a function of frequency and of mode of generation. A parameter of interest will be the substrate material. Concurrently, an x-ray analysis will be attempted in order to determine the stoichiometry of the films and its correlation with the piezoelectric efficiencies for the different modes of generation.

R. Weber  
J. W. Burke

## 2. Microwave Phonon Generation

Longitudinal phonon echoes have been observed for the first time at 70 GHz using 1600-Å thick CdS film transducers, which were deposited on quartz by R. Weber and J. W. Burke (Sec. IV-B-1). The measured velocity in quartz of  $6.25 \times 10^5$  cm/sec agrees within experimental error with the value reported in the literature for the velocity of the longitudinal mode in the z-direction. Four echoes were observed, with the first echo 6 dB above noise level. Although the overall efficiency of the transduction process for this particular quartz sample and CdS film is less than that usually observed for x-cut quartz, no general statement can be made about the performance of CdS films without testing at least several samples. Successful development of this technique will allow an investigation of the propagation of sound in z-cut quartz, c-axis sapphire, and other nonpiezoelectric materials.

J. B. Thaxter  
C. D. Parker

## C. MAGNETISM

### 1. Magnetic Properties of Chromium Spinels with Nonmagnetic A-Sites

Study of the magnetic properties of the spinels  $ACr_2X_4$ , where A is nonmagnetic zinc or cadmium and X is oxygen, sulfur, or selenium, first reported in the previous Solid State Research Report,<sup>8</sup> has been continued. We have found that  $CdCr_2S_4$ , like  $CdCr_2Se_4$ , is ferromagnetic with a moment of  $5.55 \mu_B$  at 4.2°K in 10,000 oe, a Curie temperature  $T_C = 86^\circ K$ , a Curie-Weiss constant  $C_M = 3.75$ , and an asymptotic Curie point  $T_A = 156^\circ K$ . We had found that  $CdCr_2O_4$  becomes antiferromagnetic below  $T_N = 9^\circ K$ .<sup>8</sup> Measurements of the paramagnetic behavior show that  $C_M = 3.54$  and  $T_A = -88^\circ K$  in this material.

The effect of cell size on  $T_A$  in the entire series of compounds is shown in Fig. IV-8. It can be seen that there is a strong dependence of  $T_A$  on lattice size for either A-site ion, but that the quantitative variation is quite different depending on whether the A-site ion is zinc or cadmium. Since  $T_A$  is proportional to the sum of all the magnetic exchange interactions, this further indicates that the diamagnetic A-site cation significantly affects these interactions. Specifically, the data shown in Fig. IV-8 indicate that for a given cell size, the substitution of cadmium for zinc tends to reduce the antiferromagnetic next-nearest-neighbor interaction, or to increase the ferromagnetic nearest-neighbor interaction, or both. This conclusion is consistent with the relatively low Néel temperature in  $CdCr_2O_4$  and with the advent of ferromagnetism in the cadmium-chromium chalcogenides.

## Section IV

Although it would be attractive to assume that the A-sites are directly involved in the next-nearest-neighbor interactions of the type Cr-anion-A-site-anion-Cr, our results cannot rule out an alternative explanation wherein the A-sites play only an indirect role in Cd-anion-anion-Cr interactions by affecting the electron distribution of the anions.

N. Menyuk R. J. Arnett  
K. Dwight A. Wold†

### 2. Reduced Manganese Moment in Manganese Chromite

The following is an abstract of a paper which is being presented at the 11th Annual Conference on Magnetism and Magnetic Materials, San Francisco, California:

"The net magnetization, magnetic susceptibility,  $Mn^{55}$  nuclear magnetic resonance, and neutron diffraction properties of  $MnCr_2O_4$  have been reinvestigated. Our results are in general agreement with earlier findings. The neutron diffraction pattern of  $MnCr_2O_4$  evidences appreciable deviation from a pure spiral configuration. Furthermore, the susceptibility data indicate that the  $Mn^{++}$  ions possess a reduced magnetic moment of about  $4.3 \mu_B$ , rather than the previously assumed value of  $5.0 \mu_B$ . Given the hypothesis of an admixture of quartet states with quenched orbital momentum into the  $^6S$  free-ion ground state, the reduced value of the  $Mn^{55}$  hyperfine field observed in manganese chromite is consistent with this low value for the manganese moment.

"The interpretation of the NMR result in terms of a ferrimagnetic spiral ground-state spin configuration remains essentially unchanged, a manganese cone angle of about  $61^\circ$  being indicated. The use of  $4.3 \mu_B$  for the  $Mn^{++}$  moment improves the agreement between the theoretical and observed neutron diffraction patterns, but the best fit is still obtained with a much smaller value for this cone angle, namely  $33^\circ$ . Within the spiral model, the observed magnetic diffraction intensities are incompatible with the larger cone angle; the NMR findings are incompatible with the smaller. Other discrepancies are also discussed."

K. Dwight J. Feinleib  
N. Menyuk A. Wold†

### 3. Temperature Variation of Spin Wave Dispersion Relation

In previous experiments,<sup>9</sup> the long-range interaction  $\langle \rho^2 \rangle$  was obtained from the ratio of the coefficient of the quartic term  $F$  to the coefficient of the quadratic term  $D$  in the spin wave dispersion relation  $\epsilon_k = Dk^2 - Fk^4$  by spin wave measurements at 70 GHz on permalloy at 298°, 77°, and 4.2°K. Similar measurements have now been completed over a temperature range of 4.2° to 300°K at 61.8 GHz.

The measurements are of interest because the dispersion relation and hence  $\langle \rho^2 \rangle$  are obtained for the same temperature range over which spin wave interactions and magnetization measurements have been found to follow spin wave theory. In addition, the temperature dependence of  $F$ , which can be related to a  $T^{7/2}$  term in the temperature dependence of the exchange parameter  $D$ , is obtained.

---

† Engineering Department, Brown University.

The experimental method and the procedure for analyzing the data were the same as previously described. The apparatus was modified to include a triple dewar system which allowed temperature control from 4.2° to 298°K by means of an exchange gas. The magnetic field was measured by means of an NMR probe.

It was found that on a 63% Ni-37% Fe film, 6950 Å thick, the coefficients of both the quadratic and the quartic terms vary as  $T^{5/2}$  up to 80°K and approximately as  $T^{3/2}$  up to 298°K. This is the same behavior previously reported<sup>10</sup> for the quadratic term using a different permalloy film at 9 GHz. These results indicate that  $\langle \rho^2 \rangle$  varies as  $T^{5/2}$  over the low temperature range, and that the range increases by 10 percent from 298° to 4.2°K.

R. Weber  
P. E. Tannenwald  
J. W. Burke

#### 4. On Marshall's General Spin Wave Theory

Marshall<sup>11</sup> has given the following beautifully simple and fairly general model for treating a system of interacting spin waves. Suppose we assume that spin waves are bosons described by occupation numbers  $n_k$  ( $= 0, 1, 2, \dots$ ,  $k$  going over a Brillouin zone), and that in the energy eigenstates (or approximate energy eigenstates) of the system of interest, these  $n_k$  are good quantum numbers. Then the energy levels (or approximate energy levels) of the system are functions of the  $n_k$ ; for noninteracting spin waves these would be linear functions and for low-lying levels (small  $n_k$ ) one expects the expansion

$$E(\{n\}) = \sum_q n_q \epsilon_q - \sum_{qp} n_q n_p c_{qp} + \dots \quad (3)$$

to be valid. Following Marshall, we neglect all other types of excitations — this means that  $\epsilon_q, c_{qp}, \dots$  are constants (independent of temperature  $T$ ) and the energy levels  $E$  are completely specified by these  $n_k$ .

The spin wave excitation energy is defined as

$$\epsilon_k \equiv \langle E(\dots, n_k + 1, \dots) - E(\dots, n_k, \dots) \rangle \quad (4)$$

where  $\langle f(\{n\}) \rangle \equiv \sum_{\{n\}} f(\{n\}) \exp[-\beta E(\{n\})] / \sum_{\{n\}} \exp[-\beta E(\{n\})]$ , and  $\beta = 1/(kT)$ . Assuming finally that  $\epsilon_k = Dk^2 + Fk^4 + \dots$  as  $k \rightarrow 0$ , Marshall deduced the  $T^{5/2}$  temperature dependence of  $D$ .

We have simply followed this argument to find the higher-order terms occurring in  $D$  as well as the temperature dependence of  $F$  (this involves the additional assumption that the terms in  $\epsilon_k$  of order  $k^4$  are spherically symmetric). We obtained

$$D = D_0 (1 - GT^{5/2} + LT^{7/2} + \dots)$$

$$F = F_0 (1 - HT^{5/2} + \dots) \quad (5)$$

The first interesting result is the prediction that  $F$  should also show a  $T^{5/2}$  dependence. This was subsequently found to be the case in permalloy films by Weber, Tannenwald, and Burke (Sec. IV-C-3). We also noticed that the coefficients  $G, L, \dots, H, \dots$  are, surprisingly, not linearly

## Section IV

independent; in fact an explicit relation between G, L, and H follows from the above considerations and is conveniently summarized by

$$\frac{LT^{7/2}}{GT^{5/2}} = \kappa T \frac{35F_0}{4D_0^2} \frac{\zeta(7/2)}{\zeta(5/2)} \left(1 + \frac{2}{7} \frac{H}{G}\right) \quad (6)$$

where  $\zeta(5/2) = 1.344$ ,  $\zeta(7/2) = 1.127$  (Riemann  $\zeta$ -functions). This will allow an estimate of the size of the  $T^{7/2}$  term and hence will indicate if this term can be determined with the present experimental data.

T. A. Kaplan  
H. E. Stanley

## 5. Light Scattering from Spin Fluctuations in Ferromagnets

Large cross sections have been calculated for light scattering from long wavelength spin fluctuations in ferromagnets near the Curie temperature. The spin fluctuations, which appear as magnetization fluctuations, modulate the optical dielectric tensor components which ordinarily produce the large Faraday and Kerr effects below the Curie point.

Scattering in the present model is caused by the interband optical dipole transitions between 3d and excited s bands, which are perturbed by a spin-orbit interaction which fluctuates because of spin-spin interaction. The results can be readily extended to the case of localized states in crystals. Assuming that the spin-orbit and electromagnetic interaction can be treated as first-order perturbations, and the spin fluctuations due to exchange forces can be decoupled from the spatial wave functions in the unperturbed system, the cross section  $\sigma$  for light scattering in the frequency range  $d\omega$  and solid angle range  $d\Omega$  is

$$\frac{d^2\sigma}{d\omega d\Omega} = r_0^2 \frac{\omega}{\omega_0} \underline{\underline{f}} : \underline{\underline{C}}(\underline{q}, \omega_0 - \omega) \quad (7)$$

where  $r_0$  is the classical electron radius, and  $\omega$  and  $\omega_0$  are the frequencies of the scattered and incident light, respectively. The electromagnetic spin-independent tensor form factor,  $\underline{\underline{f}}$ , is given in the dipole approximation by

$$\underline{\underline{f}} = \sum_{\substack{d, s \\ \text{BZ}}} (f_d - f_s) \left\{ \sum_{d'} \frac{\underline{A} \cdot \underline{P}_{ds} \underline{P}_{sd'} \cdot \underline{A}_0 (\hbar \nabla V(r) \times \underline{P})_{d'd}}{2m^3 c^2 [E_{sd} + \hbar(-\omega_0 + i\Gamma_{ds})] [E_{dd'} + \hbar(\omega_0 - \omega - i\Gamma_{d'd})]} \right. \\ \left. + \dots \right\} \text{ (complex conjugate)} \quad (8)$$

where  $\underline{A}$  and  $\underline{A}_0$  are the unit polarization vectors of the scattered and incident light, with wave vectors  $\underline{K} + \underline{q}$  and  $\underline{K}$ , respectively. The Fermi factors for the d and s bands, neglecting the exchange energy splitting, are  $f_{d, s}$ . The spin-spin correlation tensor Fourier component of wave vector  $\underline{q}$  and frequency  $\omega_s$  is  $\underline{\underline{C}}(\underline{q}, \omega_s)$ . By the fluctuation-dissipation theorem,

$$\underline{\underline{C}}(\underline{q}, \omega_s) = N \text{Im} \underline{\underline{\chi}}(\underline{q}, \omega_s) \hbar [\coth(\hbar\omega_s/2kT) \mp 1] / 8\pi\mu_B^2 \quad \text{for } \omega_s \lesssim 0$$

where  $\underline{\underline{\chi}}$  is the dynamic magnetic susceptibility and N is the total number of spins in the crystal.

At low temperatures, magnon and optical spin waves cause fluctuations peaked about values of  $\omega_s$  given by their respective dispersion curves  $\omega_s(\underline{q})$ .

Estimates of this cross section can be obtained from the dielectric tensor  $\underline{\epsilon}$  below the Curie temperature, namely,

$$\underline{\epsilon}(\underline{K}, \omega) = A_0 \underline{I} - A_1 \underline{I} \times \text{Tr } \rho^0 \underline{S} \quad (9)$$

Then, with  $V$  denoting the unit cell volume, we obtain

$$\frac{d^2 \sigma}{d\omega d\Omega} \approx |A_1 V|^2 \frac{\omega_0^3 \omega}{c^4 (4\pi)^2} C_{zz}(\underline{q}, \omega_s = \omega_0 - \omega) \quad (10)$$

By integrating over angle and frequency and using the Kramers-Kronig theorem, the total cross section, in the high temperature limit, becomes

$$\sigma \approx \frac{|A_1 V|^2}{6\pi} \frac{\omega_0^4}{c^4} N X_{\underline{q}}(T) \quad (11)$$

where

$$X_{\underline{q}}(T) = \text{Re } \chi(\underline{q}, 0) (kT/4\mu_B^2) \underset{T \rightarrow T_c}{\sim} \frac{S(S+1)/3}{\left(\frac{T-T_c}{T}\right)^\gamma + (a\underline{q})^2 + \dots}$$

The Faraday and Kerr effects on transmitted or reflected light are proportional to  $A_1$ . For example, it is known that for nickel and iron,  $\text{Re } A_1 \approx \text{Im } A_1 \approx 0.1$ . For  $(T - T_c)/T \approx 10^{-4}$  (corresponding to temperature control of within  $0.1^\circ\text{K}$ ),  $\gamma \approx 4/3$  (corresponding to measurements of the long wavelength susceptibility), and  $(a\underline{q})^2 \approx 10^{-4}$  (corresponding to an exchange interaction length  $a$  of about  $10\text{\AA}$ ), Eq. (11) yields a cross section  $\sigma \approx 10^{-3} \text{cm}^2$ . Thus, an incident power of  $1 \text{W/cm}^2$  results in a total of a milliwatt of scattered power from a cubic centimeter of illuminated crystal. Scattering of a transmitted beam could be observed in transparent ferromagnetic crystals, such as YIG,  $\text{CrBr}_3$ , and  $\text{EuS}$ , whereas scattering of a reflected beam could be observed from ferromagnetic conductors, such as nickel and iron.

The frequency spectrum of the spin fluctuations is expected to become sharply peaked at zero frequency, like Rayleigh scattering in critical liquids, because of the large susceptibility near the Curie temperature. According to neutron scattering measurements on iron, the spectral width  $\Delta\omega$  varies as  $D [q^2 + \text{const}(T - T_c)]$ . Since  $D \approx 2 \times 10^{-3} \text{cm}^2/\text{sec}$ , the width may be a few megacycles or less, which is suitable for laser "self-beating" experiments.

M. M. Litvak  
H. J. Zeiger

## 6. Paramagnetic Spin Waves in Superconductors

A gas of interacting electrons has certain modes of oscillation of high phase velocity called "zero sound." The term was coined by Landau who first discovered them. Since Landau proposed their existence, they have remained experimentally undetected. Our interest is in a subclass of these oscillations which seems to offer the greatest possibility of being detected in actual materials. This class of modes is characterized by propagating spin density variations. We find that

## Section IV

materials which exhibit superconductivity are far more likely candidates for the detection of these modes; we propose two experiments, the first modeled on a conventional thin-film spin wave resonance experiment, and the second, a more elaborate film transmission experiment. The second is designed to observe an effect of the electronic orbital motion, a magnetic field induced rotation of the wave fronts of the propagating spin wave.

Because certain features of the problem may be solved without recourse to approximation, the study of these modes illuminates some features of collective mode theory in general. In particular, while the excited states of a system described by an Hermitian Hamiltonian have infinite lifetimes, approximate theory and experiments generally find finite lifetimes and nonzero resonance linewidths. The difference between these points of view and the resolution of the apparent paradox may be very clearly seen in studying the paramagnetic spin wave.

L. L. Van Zandt

### D. QUANTUM TRANSPORT THEORY

#### 1. Pseudomomentum of Phonons

A simple and general treatment of the role of  $\hbar\vec{q}$ , where  $\vec{q}$  is the wave vector of a normal mode of vibration of a lattice, as a pseudomomentum of the phonon has been found by considering the transformation properties of the vibrating system under the unitary operator.

$$C(\vec{x}) = \exp[-i\vec{K} \cdot \vec{x}/\hbar] \quad , \quad (12)$$

corresponding to the Hermitian operator

$$\vec{K} = \sum_{\vec{q}\kappa} \hbar\vec{q} b_{\vec{q}\kappa}^{\dagger} b_{\vec{q}\kappa} \quad , \quad (13)$$

where  $b$  and  $b^{\dagger}$  are the destruction and creation operators for the phonons.

For the anharmonic lattice, i.e., interacting phonons, it is easy to see that the Hamiltonian is invariant under the unitary transformation  $C(\vec{a}_m)$ , where  $\vec{a}_m$  is a lattice vector, i.e.,  $C(\vec{a}_m) H C^{-1}(\vec{a}_m) = H$ . Thus,  $C(\vec{a}_m)$  is a constant of the motion,  $[C(\vec{a}_m), H] = 0$ . If now we write  $H = H_0 + H_1$ , where

$$H_0 = \sum_{\vec{q}\kappa} \hbar\omega_{\vec{q}\kappa} (b_{\vec{q}\kappa}^{\dagger} b_{\vec{q}\kappa} + \frac{1}{2}) \quad (14)$$

is the Hamiltonian for the harmonic part of the vibrations and  $H_1$  the phonon-phonon interaction, we have

$$[C(\vec{a}_m), H_1] = 0 \quad (15)$$

since  $C(\vec{a}_m)$  clearly commutes with  $H_0$ . In a representation in which all  $b_{\vec{q}\kappa}^{\dagger} b_{\vec{q}\kappa}$  are diagonal, Eq. (15) gives

$$\left\{ \exp \left[ -\frac{i}{\hbar} \vec{K} \{n_{\vec{q}\kappa}\} \cdot \vec{a}_m \right] - \exp \left[ -\frac{i}{\hbar} \vec{K} \{n'_{\vec{q}\kappa}\} \cdot \vec{a}_m \right] \right\} \langle \{n_{\vec{q}\kappa}\} | H_1 | \{n'_{\vec{q}\kappa}\} \rangle = 0 \quad (16)$$

Thus, for all processes possible due to the phonon-phonon interaction  $H_1$ , we must have the selection rule

$$\vec{K} \{n_{\vec{q}\kappa}\} = \vec{K} \{n'_{\vec{q}\kappa}\} + \hbar \vec{b}_{\vec{n}} \quad (17)$$

where  $\vec{b}_{\vec{n}}$  is a reciprocal lattice vector. Thus, we have

$$\sum_{\vec{q}\kappa} \vec{q} n_{\vec{q}\kappa} = \sum_{\vec{q}\kappa} \vec{q} n'_{\vec{q}\kappa} + \vec{b}_{\vec{n}} \quad (18)$$

which exhibits the pseudomomentum character of  $\hbar \vec{q}$  for each phonon.

A similar treatment can be given for the harmonic crystal interacting with an external system which cannot distinguish between the crystal particles. This system can be proved to be invariant under  $C(\vec{a}_m)$  and a simultaneous translation of the external system by  $\vec{a}_m$ . This leads in an analogous way to

$$\vec{p} + \sum_{\vec{q}\kappa} \hbar \vec{q} n_{\vec{q}\kappa} = \vec{p}' + \sum_{\vec{q}\kappa} \hbar \vec{q} n'_{\vec{q}\kappa} + \hbar \vec{b}_{\vec{n}} \quad (19)$$

where  $\vec{p}$  and  $\vec{p}'$  are the momenta of the external system in its "initial" and "final" states.

Note that the transformation by  $C(\vec{a}_m)$  does not translate the particles. The operator that generates the translation is, of course, the total momentum of the lattice. This leads to the familiar conservation of the total momentum, in addition to Eqs. (18) and (19). The main point here has been anticipated in the work of G. Sussmann.<sup>12</sup>

P. N. Argyres

## 2. Polaron Energy Spectrum

The energy spectrum of a polaron — an electron interacting with the longitudinal optical phonons of a polar crystal — has been studied, with particular attention given to the region where the polaron excitation energy closely approaches the energy of a longitudinal optical phonon. In this region, existing theories of the polaron spectrum are inadequate; in particular, the usual Rayleigh-Schrodinger perturbation theory is shown to be inconsistent.

A self-consistent weak coupling theory and a variational theory of the polaron spectrum which, for small coupling, reduces to this weak coupling theory, have been developed.

Schultz<sup>13</sup> and Whitfield and Puff<sup>14</sup> have conjectured that the polaron energy  $E(p)$  bends over and becomes horizontal as the polaron momentum,  $p$ , approaches from below the value at which the polaron excitation energy,  $E(p) - E(0)$ , becomes equal to the optical phonon energy. Using the above-mentioned weak coupling method, this conjecture has been verified to lowest order and next higher order in the coupling constant.

D. M. Larsen

## 3. Quantum Theory of Kinetic Equations for Electrons in Random Impurities

We have considered the problem of deriving kinetic equations for electrons under the action of arbitrary space-time varying driving fields and randomly distributed impurities from a fresh

## Section IV

point of view. We first derive a kinetic equation for the whole one-electron density operator by eliminating the dependence on the positions of the impurities, using a general procedure reported earlier by Argyres.<sup>15</sup>

From this general kinetic equation we can then easily derive special kinetic equations for the subsets of the one-electron density matrix appropriate to special situations. For example, the usual Boltzmann transport equation for the distribution function is derived, without the additional assumptions or theorems necessary in earlier theories. The appropriate kinetic equation when a quantizing magnetic field is present is also easily deduced.

The theory of power absorption by direct and indirect processes is developed on the basis of the general kinetic equation.

The case of an inhomogeneous electromagnetic field is considered in detail, with emphasis on the requirements of gauge invariance and the conditions necessary for the commonly assumed form of the Boltzmann equation for the space-varying distribution function.

A full report of the work is being prepared for publication.

P. N. Argyres  
E. S. Kirkpatrick

### 4. Quasi-Photons in Charged Media

The interaction of photons with charged particles leads in the zeroth approximation to quasi-photons with dispersion given by

$$\omega_{\vec{k}}^2 = c^2 k^2 + \omega_p^2, \quad (20)$$

where  $\omega_p$  is the plasma frequency of the charged particles. This relation has recently been derived<sup>16</sup> by the method of Bogoliubov and Tyablikov and also by the method of the equation of motion.

We have proved relation (20) in a simple way without any transformation, by first writing the Hamiltonian for the system not in terms of the creation and destruction operators for the bare photons and the charged particles, but, instead, in terms of the complex normal coordinates of the fields. It is then immediately obvious that in addition to the "potential" energy of the bare photons

$$\sum_{\vec{k}\lambda} c^2 k^2 A_{\vec{k}\lambda}^+ A_{\vec{k}\lambda}, \quad (21)$$

there is a similar term in the Hamiltonian due to the  $\bar{A}^2$ -term of the interaction of the radiation field with the mean number of the charged particles. This term can be written in terms of the complex normal coordinates as

$$\sum_{\vec{k}\lambda} \omega_p^2 A_{\vec{k}\lambda}^+ A_{\vec{k}\lambda}, \quad (22)$$

which combines with the previous term of the bare photons to give the renormalized photons with dispersion given by Eq. (20).

P. N. Argyres

## REFERENCES

1. J. C. Slater and G. F. Koster, *Phys. Rev.* 94, 1498 (1954).
2. J. B. Goodenough, *Bull. Soc. Chim. France*, 1200 (1965), DDC 618458.
3. J. C. Slater, *Phys. Rev.* 51, 846 (1937).
4. Solid State Research Report, Lincoln Laboratory, M. I. T. (1965:2), pp. 53-55, DDC 624611.
5. *Ibid.* (1965:1), p. 74, DDC 622446, H-678.
6. J. M. Luttinger, *Phys. Rev.* 102, 1030 (1956).
7. M. S. Dresselhaus and J. G. Mavroides, *Phys. Rev. Letters* 14, 259 (1965), DDC 614312.
8. Solid State Research Report, Lincoln Laboratory, M. I. T. (1965:2), pp. 60-63, DDC 624611.
9. *Ibid.* (1965:1), p. 71, DDC 622446, H-678; (1965:2), p. 60, DDC 624611.
10. R. Weber and P. E. Tannenwald, *J. Phys. Chem. Solids* 24, 1357 (1963).
11. W. Marshall, *Proc. Eighth International Conference on Low Temperature Physics*, London, 1962 (Butterworths, London, 1963).
12. G. Sussmann, *Z. Naturforsch.* 11a, 1 (1956), and 13a, 1 (1958).
13. T. D. Schultz, Technical Report 9, Solid State and Molecular Theory Group, M. I. T. (1956), unpublished.
14. G. Whitfield and R. Puff, *Phys. Letters* 10, 9 (1964).
15. P. N. Argyres, *Lectures in Theoretical Physics*, Boulder, Colorado, Vol. VIII (1965), to be published.
16. W. R. Chappell and W. E. Brittin, *Nuovo cimento* 38, 1187 (1965).

**DOCUMENT CONTROL DATA - R&D**

*(Security classification of title, body of abstract and indexing annotation must be entered when the overall report is classified)*

1. ORIGINATING ACTIVITY <i>(Corporate author)</i>  Lincoln Laboratory, M. I. T.		2a. REPORT SECURITY CLASSIFICATION Unclassified	
		2b. GROUP None	
3. REPORT TITLE  Solid State Research			
4. DESCRIPTIVE NOTES <i>(Type of report and inclusive dates)</i> Quarterly Technical Summary - 1 August 1965 through 31 October 1965			
5. AUTHOR(S) <i>(Last name, first name, initial)</i>  McWhorter, Alan L.			
6. REPORT DATE 15 November 1965		7a. TOTAL NO. OF PAGES 72	7b. NO. OF REFS 70
8a. CONTRACT OR GRANT NO. AF 19 (628)-5167		9a. ORIGINATOR'S REPORT NUMBER(S) Solid State Research (1965:3)	
b. PROJECT NO. 649L		9b. OTHER REPORT NO(S) <i>(Any other numbers that may be assigned this report)</i> ESD-TDR-65-553	
c.			
d.			
10. AVAILABILITY/LIMITATION NOTICES  Distribution of this document is unlimited.			
11. SUPPLEMENTARY NOTES  None		12. SPONSORING MILITARY ACTIVITY  Air Force Systems Command, USAF	
13. ABSTRACT  This report covers in detail the solid state research work at Lincoln Laboratory for the period 1 August through 31 October 1965. The topics covered are Solid State Device Research, Laser Research, Materials Research, and Physics of Solids.			
14. KEY WORDS			
solid state devices	reflectivity	magnetoabsorption	pressure dependence
solid state physics	solution regrowth	cyclotron resonance	magnetism
laser research	injection mechanisms	hypersonic waves	light scattering
materials research	microwave amplifiers	high power Brillouin scattering	pseudomomentum
pressure tuning	optical beams	high power Raman scattering	
wet chemical analysis	high power laser	photoelectron statistics	
electronic band structure	transition-metal compounds	thermodynamic studies	



